
Article:
Xu, J., Odavic, M. orcid.org/0000-0002-2104-8893, Zhu, Z.-Q. orcid.org/0000-0001-7175-3307 et al. (2 more authors) (2021) Modulation restraint analysis of space vector PWM for dual three-phase machines under vector space decomposition. IEEE Transactions on Power Electronics, 36 (12). pp. 14491-14507. ISSN 0885-8993

https://doi.org/10.1109/tpel.2021.3089006

Modulation Restraint Analysis of Space Vector PWM for Dual Three-Phase Machines Under Vector Space Decomposition

Jin Xu, Milijana Odavic, *Member, IEEE*, Zi-Qiang Zhu, *Fellow*, *IEEE*, Zhan-Yuan Wu, and Nuno Freire

***Abstract*—For dual three-phase machines, vector space decomposition allows the control of fundamental and main harmonic components in αβ and xy subspaces, respectively. However, the modulation of voltage references in the two subspaces using the space vector pulse width modulation (SVPWM) is not independent but coupled. In that, voltage references of two subspaces cannot be modulated simultaneously beyond the modulation restraints, thereby distorting the voltage regulation and causing harmonics or even system misbehavior. Meanwhile, the fundamental voltage in αβ subspace responsible for electromagnetic torque generation should be prioritized and secured. Thus, this paper proposes a systematic analysis of modulation restraints of three representative SVPWM techniques, i.e. the linear modulation range of xy subspace under an assured modulation index of the fundamental voltage. Voltage references of xy subspace within this range can be modulated successfully without affecting the assured modulation index and the margin left for harmonic control in xy subspace is then acknowledged. This can be used to limit the output of current controllers not to exceed the voltage modulation restraint, thereby avoiding the modulation failure. Finally, the experimental results validate the linear modulation range and demonstrate the modulation behaviors within and out of the linear modulation range.**

***Index Terms*— Dual three-phase machines, modulation restraint, space vector pulse width modulation, vector space decomposition.**

NOMENCLATURE

θ_e	Electrical angular position.
ω_e	Electrical angular speed.
R_s	Stator resistance.
T_{PWM}	PWM period.
T_e	Electromagnetic torque.
V_{dc}	DC-link voltage.
D_R, D_S, D_T, D_U, D_V, D_W	Duty cycles of phases.
i_R, i_S, i_T, i_U, i_V, i_W	Phase currents.
u_R, u_S, u_T, u_U, u_V, u_W	Phase voltages.
u_α, u_β; i_α, i_β; $L_{\alpha e}$, $L_{\beta e}$; ψ_α, ψ_β	Voltages, currents, inductances, and flux linkages in αβ subspace.
u_x, u_y; i_x, i_y; L_x, L_y; ψ_x, ψ_y	Voltages, currents, inductances, and flux linkages in xy subspace.
ψ_{fd}	Rotor flux linkage
$\boldsymbol{V}_{\boldsymbol{\alpha\beta}}^{(*)} = \left[u_\alpha^{(*)} \quad u_\beta^{(*)}\right]^{\mathrm{T}}$, $\boldsymbol{V}_{\boldsymbol{xy}}^{(*)} = \left[u_x^{(*)} \quad u_y^{(*)}\right]^{\mathrm{T}}$	Modulated (Reference) voltage vectors in αβ, xy subspaces.
$\left\|\boldsymbol{V}_{\boldsymbol{\alpha\beta}}^{(*)}\right\|$, $\left\|\boldsymbol{V}_{\boldsymbol{xy}}^{(*)}\right\|$	Lengths of $\boldsymbol{V}_{\boldsymbol{\alpha\beta}}^{(*)}$ and $\boldsymbol{V}_{\boldsymbol{xy}}^{(*)}$
P	Number of pole pairs

This work was supported by the UK EPSRC Prosperity Partnership "A New Partnership in Offshore Wind" under Grant No. EP/R004900/1."

Jin Xu, Milijana Odavic and Zi-Qiang Zhu are with Department of Electronic and Electrical Engineering, University of Sheffield, Sheffield, U.K. (e-mail: jxu60@sheffield.ac.uk; m.odavic@sheffield.ac.uk; z.q.zhu@sheffield.ac.uk). Zhan-Yuan Wu is with Sheffield Siemens Gamesa Renewable Energy Research Centre, Sheffield, U.K. (e-mail: Zhan-Yuan.Wu@siemensgamesa.com). Nuno Freire is with Siemens Gamesa Renewable Energy AS, Brande, Denmark. (e-mail: Nuno.Freire@siemensgamesa.com).

I. INTRODUCTION

DUAL three-phase (3-ph) machines have seen an increasing trend of applications in industries[1]-[6], because of advantages such as high torque density, high-power low-current capability, etc. There is one more set of 3-ph windings with respect to single 3-ph machines and therefore two sets of 3-ph windings can be controlled separately, viewed as two 3-ph machines [7]-[8]. However, the challenge of this control structure is the coupling issue of mutual inductance between phases from two sets, respectively. To achieve a completely decoupled machine model, vector space decomposition (VSD) [9] is developed for dual 3-ph machines, in which two sets of 3-ph windings are modelled into two-dimensional orthogonal αβ and xy subspaces. The outstanding benefit of VSD is the mutual inductance between phases from two sets, respectively, can be decoupled. Furthermore, the fundamental component and harmonics with $12k\pm1$ (k=1,2,3⋯) order are decoupled into αβ subspace, while harmonics with $6k\pm1$ (k=1,3,5⋯) order are mapped into xy subspace. This will allow components with different orders to be controlled separately.

The fundamental components in αβ subspace need to be well regulated to satisfy the torque requirement and the amplitudes of the $12k\pm1$ (k=1,2,3⋯) harmonics are normally much lower. Meantime, the harmonics in xy subspace deserve good suppression as well to improve machine performances, such as low THD, small torque ripple, etc. Due to inverter nonlinearities and emf distortion, the 5th and 7th order harmonics are excited and then decoupled in xy subspace [10]-[11]. Additionally, impedance asymmetries would lead to fundamental order currents in xy subspace as well [11]. To balance phase currents, they should be suppressed. Thus, the control of xy subspace is of importance.

Due to the advantages mentioned above, many advanced control strategies are developed based on VSD [9],[12]-[20], in which, the space vector pulse width modulation (SVPWM) is implemented to modulate voltage references of αβ and xy subspaces into the switching pattern providing gate signals of power devices. A simplified drive structure is shown in Fig. 1. The dual 3-ph machine has two sets of 3-ph windings (Set 1 and Set 2) with 30° angle displacement. From Fig. 1, no matter what control strategies are implemented, the SVPWM technique should transfer voltage references into the switching pattern correctly, thereby controlling the machine.

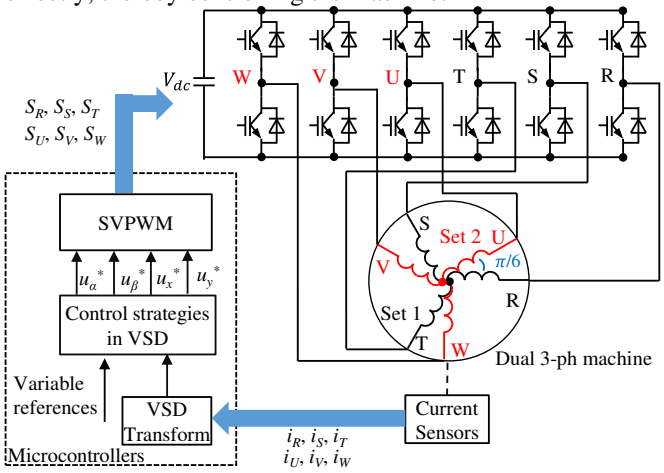

Fig. 1 Simplified drive structure of dual 3-ph machine under VSD.

However, one challenge is how to select active voltage vectors from a total number of 64 vectors to conduct the modulation during each PWM period. It should be noted that the selection principle determines the modulation restraint and computation burden. From the literature, there are mainly three categories of SVPWM techniques for dual 3-ph machines regarding the voltage vector selection principle. In [9], [12]-[15], four of twelve longest voltage vectors in αβ subspace are selected in each PWM period to modulate the αβ subspace voltage reference with the average zero voltage achieved in xy subspace, resulting in no closed-loop current control capability in xy subspace. Another SVPWM technique is to modulate the voltage references in two separate 3-ph frames using classical SVPWM developed for 3-ph machines [16]-[19]. The voltage references of two subspaces need to be transformed to voltage references in two 3-ph frames. Besides, synthetic vectors can be implemented to modulate the voltage references in two subspaces, respectively, without the coupling of dwell times [20]. Each PWM period is divided into two parts, responsible for modulations in two subspaces, respectively. Therefore, the division plays a significant role in determining the modulations of voltage references in two subspaces. However, the switching sequence generation is much complicated and the multiple switching issue could increase the switching losses.

The major concern of applying these SVPWM techniques is whether voltage references of two subspaces can be modulated simultaneously and successfully, due to the reason that the modulations of two subspaces are coupled by dwell times of voltage vectors. The coupling of modulations in two subspaces, or generally the modulation restraints of these SVPWM techniques, are not discussed in the literature. In the control loop, the voltage references in both αβ and xy subspaces should be modulated into pulses and then be delivered to phase terminals, thereby controlling the dual 3-ph machine. Theoretically, neither of the two voltages references can be sacrificed, since the αβ voltage reference (fundamental voltage reference) controls the output of the electromagnetic torque and the xy voltage reference is in charge of harmonic regulation. However, the literature [9], [12]-[20] focuses on the development of SVPWM techniques, in other words, the generation of pulses according to the reference, rather than the modulation restraint of the two voltage references. It is not considered in the literature that voltage references of two subspaces beyond the modulation restraint cannot be modulated, thereby distorting the voltage regulation and causing harmonics or even system misbehavior.

Therefore, this paper aims to analyze the modulation restraint of SVPWM techniques under VSD to assure that the voltage references, which are conventionally outputs of current controllers, will not exceed the modulation restraint, thereby avoiding the modulation failure. The main contribution is to propose a systematic and practical analysis of the modulation restraint, i.e. the linear modulation range of xy subspace under an assured modulation index of the fundamental voltage. Unless voltage references of xy subspace are out of this range, they can be modulated successfully under an assured modulation index of the fundamental voltage. The reason to secure the modulation index is that the electromagnetic torque generation mainly relying on the fundamental current (essentially voltage) decoupled in αβ subspace should be prioritized. In any control system, the output of current controllers in xy subspace should not exceed this range, otherwise, the modulation failure could happen. From another aspect, a balanced performance can be made between the fundamental control in αβ subspace and the main harmonic control in xy subspace. If the harmonic control in xy subspace requires a large voltage, the fundamental voltage reference in αβ subspace should be reduced accordingly.

The remainder of this paper is organized as follows. The mathematical model of dual 3-ph permanent magnet synchronous machine (PMSM) used in experiments and the voltage vectors of inverters mapped into two subspaces which are vector candidates in SVPWM techniques are briefly introduced in Section II. The modulation restraints of three practical and representative SVPWM techniques are illustrated in Section III. These three SVPWM techniques include the SVPWM technique using four active vectors [9], [12]-[15], SVPWM in two separate 3-ph frames [16]-[19] and an enhanced SPVWM technique using synthetic vectors developed from [20]. In the enhanced SPVWM technique using synthetic vectors, the PWM period split is optimized by a dwell time calculation considering voltage references in two subspaces together. Compared with [20], the enhanced one is much more available and accessible for microcontrollers due to no complicated switching sequence arrangement and no multiple switching in each sapling period. Finally, the experiment results of open-loop

voltage injection and closed-loop current compensation are presented in Section IV to validate the modulation restraint.

II. Mathematical Model of Dual 3-ph PMSM and Voltage Vectors

A. Mathematical Model

Assuming sinusoidal winding distribution and neglecting core losses, magnetic saturation and asymmetric impedances, the mathematical model of dual 3-ph PMSM in VSD [9] can be expressed as (1)-(3).

$$\begin{bmatrix} u_\alpha \\ u_\beta \\ u_x \\ u_y \end{bmatrix} = \begin{bmatrix} R_s & 0 & 0 & 0 \\ 0 & R_s & 0 & 0 \\ 0 & 0 & R_s & 0 \\ 0 & 0 & 0 & R_s \end{bmatrix} \begin{bmatrix} i_\alpha \\ i_\beta \\ i_x \\ i_y \end{bmatrix} + \begin{bmatrix} \dot{\psi}_\alpha \\ \dot{\psi}_\beta \\ \dot{\psi}_x \\ \dot{\psi}_y \end{bmatrix} \tag{1}$$

$$\begin{bmatrix} \psi_\alpha \\ \psi_\beta \\ \psi_x \\ \psi_y \end{bmatrix} = \begin{bmatrix} L_{\alpha e} & 0 & 0 & 0 \\ 0 & L_{\beta e} & 0 & 0 \\ 0 & 0 & L_x & 0 \\ 0 & 0 & 0 & L_y \end{bmatrix} \begin{bmatrix} i_\alpha \\ i_\beta \\ i_x \\ i_y \end{bmatrix} + \begin{bmatrix} \cos(\theta_e) \\ \sin(\theta_e) \\ 0 \\ 0 \end{bmatrix} \psi_{fd} \tag{2}$$

$$T_e = 3P(\psi_\alpha i_\beta - \psi_\beta i_\alpha) \tag{3}$$

It can be seen from (3) that the electromagnetic torque is mainly determined by variables in αβ subspace. However, variables in xy subspace need to be controlled to improve performances such as THD reduction, torque ripple suppression, phase current balancing, etc. The control of two subspaces relies on the SVPWM using voltage vectors.

B. Voltage Vectors

As shown in Fig. 1, the two-level voltage sourced inverter (VSI) is employed. It creates 64 inverter states, corresponding to 64 voltage vectors, mapped into αβ subspace and xy subspace, shown in Fig. 2. The voltage vector numbers in Fig. 2 are defined as the decimal number values converted from the six-bit binary numbers composed of ($S_W S_V S_U S_T S_S S_R$), where $S_w, \ldots, S_R$ denote the switching states of inverter legs $W, \ldots, R$, respectively, and are either '1' (the upper power device is turning on) or '0' (the bottom power device is turning on).

The length of voltage vectors and their dwell times play a key role in the modulation procedure. As can be seen in Fig. 2, voltage vectors are divided into 4 dodecagons (N_1, N_2, N_3, N_4) regarding the voltage vector lengths, expressed as

$$\begin{cases} L_{N1} = \dfrac{\sqrt{6}-\sqrt{2}}{6} \cdot V_{dc} \\ L_{N2} = \dfrac{1}{3} \cdot V_{dc} \\ L_{N3} = \dfrac{\sqrt{2}}{3} \cdot V_{dc} \\ L_{N4} = \dfrac{\sqrt{6}+\sqrt{2}}{6} \cdot V_{dc} \end{cases} . \tag{4}$$

At each PWM period, several voltage vectors should be adopted to achieve the modulations of voltage references (outputs of current controllers) in both subspaces in SVPWM techniques, thereby controlling the machine.

III. Modulation Restraint Analysis of SVPWM Techniques

In this section, the procedure of deriving the linear modulation range reflecting the modulation restraint is explained in detail for three practical SVPWM techniques. The vector selection principles of these three SVPWM techniques are representative, which are the vector selection in two sets of 3-ph reference frames, the direct selection of four active voltage vectors, and the synthetic vector theory, respectively.

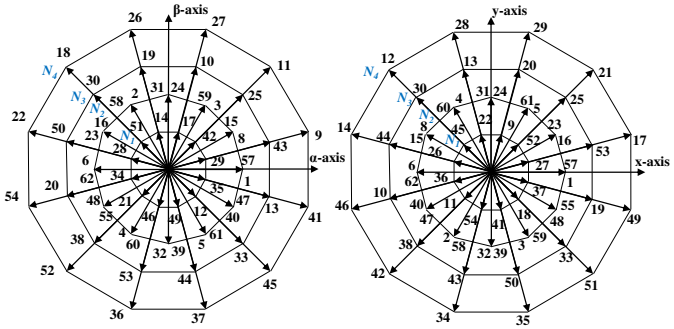

Fig. 2 Voltage vector maps. (a) αβ subspace. (b) xy subspace.

A. SVPWM with Two Separate 3-ph Modulation Frames

The diagram of SVPWM with two separate 3-ph modulation frames (SVPWM-D3) [16]-[19] is shown in Fig. 3.Voltage references $\boldsymbol{V}^*_{\alpha\beta}$ and $\boldsymbol{V}^*_{xy}$ are transformed to u_R^*, u_S^*, u_T^*, u_U^*, u_V^*, u_W^* by (5) firstly.

$$\begin{bmatrix} u_R^* \\ u_S^* \\ u_T^* \\ u_U^* \\ u_V^* \\ u_W^* \end{bmatrix} = \begin{bmatrix} 1 & 0 & 1 & 0 \\ -\frac{1}{2} & \frac{\sqrt{3}}{2} & -\frac{1}{2} & -\frac{\sqrt{3}}{2} \\ -\frac{1}{2} & -\frac{\sqrt{3}}{2} & -\frac{1}{2} & \frac{\sqrt{3}}{2} \\ \frac{\sqrt{3}}{2} & \frac{1}{2} & -\frac{\sqrt{3}}{2} & \frac{1}{2} \\ -\frac{\sqrt{3}}{2} & \frac{1}{2} & \frac{\sqrt{3}}{2} & \frac{1}{2} \\ 0 & -1 & 0 & -1 \end{bmatrix} \begin{bmatrix} u_\alpha^* \\ u_\beta^* \\ u_x^* \\ u_y^* \end{bmatrix} \tag{5}$$

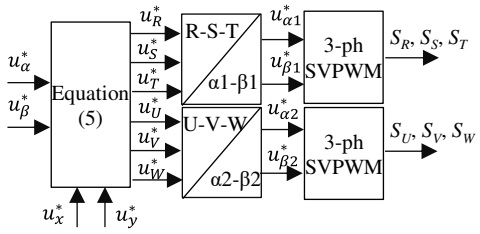

Fig. 3 Diagram of SVPWM-D3.

Then, 3-ph Clarke transform is used to derive the voltage references of Set 1 ($u_{\alpha 1}^*$ and $u_{\beta 1}^*$) in α_1-β_1 reference frame and

voltage references of Set 2 ($u^*_{\alpha 2}$ and $u^*_{\beta 2}$) in α_2-β_2 reference frame from u^*_R, u^*_S, u^*_T, u^*_U, u^*_V, u^*_W. Then, the relationship between u^*_α, u^*_β, u^*_x, u^*_y and $u^*_{\alpha 1}$, $u^*_{\beta 1}$, $u^*_{\alpha 2}$, $u^*_{\beta 2}$ is established as

$$\begin{cases} u^*_{\alpha 1} = u^*_\alpha + u^*_x \\ u^*_{\beta 1} = u^*_\beta - u^*_y \\ u^*_{\alpha 2} = \dfrac{\sqrt{3}}{2}u^*_\alpha + \dfrac{1}{2}u^*_\beta - \dfrac{\sqrt{3}}{2}u^*_x + \dfrac{1}{2}u^*_y \\ u^*_{\beta 2} = -\dfrac{1}{2}u^*_\alpha + \dfrac{\sqrt{3}}{2}u^*_\beta + \dfrac{1}{2}u^*_x + \dfrac{\sqrt{3}}{2}u^*_y \end{cases} . \quad (6)$$

The modulations of voltage references in two separate 3-ph modulation frames and modulation restrictions are presented in Fig. 4. $\boldsymbol{V^*_{\alpha 1\beta 1}} = [u^*_{\alpha 1} \quad u^*_{\beta 1}]^{\mathrm{T}}$ in α_1-β_1 reference frame and $\boldsymbol{V^*_{\alpha 2\beta 2}} = [u^*_{\alpha 2} \quad u^*_{\beta 2}]^{\mathrm{T}}$ in α_2-β_2 reference frame are modulated through conventional 3-ph SVPWM in two separate 3-ph modulation frames, respectively.

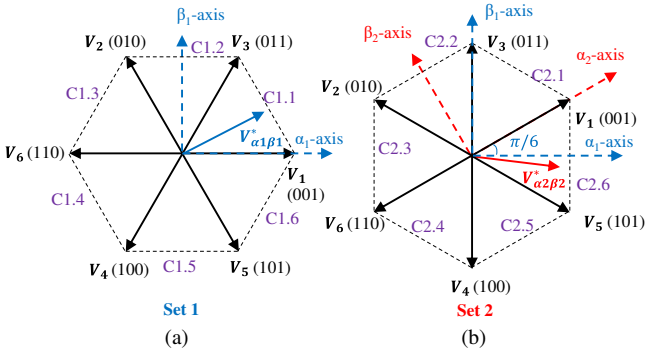

Fig. 4 Modulation restrictions in two separate 3-ph modulation frames. (a) Set 1. (b) Set 2.

From Fig. 4, $\boldsymbol{V^*_{\alpha 1\beta 1}}$ and $\boldsymbol{V^*_{\alpha 2\beta 2}}$ exceeding the modulation restrictions denoted by the dotted hexagon cannot be achieved. The restriction lines are denoted by C1.1, ⋯, C1.6 in Set 1 and C2.1, ⋯, C2.6 in Set 2, as indicated in Fig. 4. The modulation range of xy subspace in the per-unit scale with respect to V_{dc} under a given $\boldsymbol{V^*_{\alpha\beta}}$ can be derived according to these restrictions. Using $\boldsymbol{V^*_{\alpha\beta}} = \left[\frac{\sqrt{3}}{8}V_{dc} \quad \frac{1}{8}V_{dc}\right]^{\mathrm{T}}$ as an example, the derivation of the modulation range of xy subspace is presented below. The restriction line C1.1 can be expressed by $\boldsymbol{V^*_{\alpha 1\beta 1}}$ and shown as

$$-\sqrt{3}\cdot u^*_{\alpha 1} - u^*_{\beta 1} + \frac{2\sqrt{3}}{3}\cdot V_{dc} \geq 0. \quad (7)$$

Substitute (6) and $u^*_\alpha = \frac{\sqrt{3}}{8}V_{dc}$, $u^*_\beta = \frac{1}{8}V_{dc}$ into (7), the modulation restriction line in xy subspace corresponding to C1.1 in Fig. 4 can be expressed as

$$-\sqrt{3}\cdot u^*_x + u^*_y + \frac{4\sqrt{3}-3}{6}\cdot V_{dc} \geq 0, \quad (8)$$

and shown in Fig. 5(a) (marked as C1.1 accordingly). In the same way, all the modulation restriction lines in xy subspace regarding Fig. 4(a) can be obtained and shown in Fig. 5(a). Then, the distances from the point of origin to lines of C1.1, ⋯, C1.6 denoted by $d_{C1.1}$,⋯,$d_{C1.6}$ can be calculated. The distance $d_{C1.1}$ is presented in Fig. 5(a) as an example. The restriction lines regarding Fig. 4(b) in xy subspace is presented in Fig. 5(b). Similarly, the distances from the point of origin to lines of C2.1, ⋯, C2.6 denoted by $d_{C2.1}$,⋯,$d_{C2.6}$ can be calculated. Then, the modulation range of xy subspace is derived by combining Fig. 5(a) and (b), as shown in the shadowed area of Fig. 5(c). The circle indicates the linear modulation range under $\boldsymbol{V^*_{\alpha\beta}} = \left[\frac{\sqrt{3}}{8}V_{dc} \quad \frac{1}{8}V_{dc}\right]^{\mathrm{T}}$ and the magnitude (radius) denoted by L_{LMR} is calculated as $L_{LMR} = \mathrm{Min}\{d_{C1.1}, \ldots, d_{C1.6}, d_{C2.1}, \ldots, d_{C2.6}\} = 0.327 \cdot V_{dc}$.

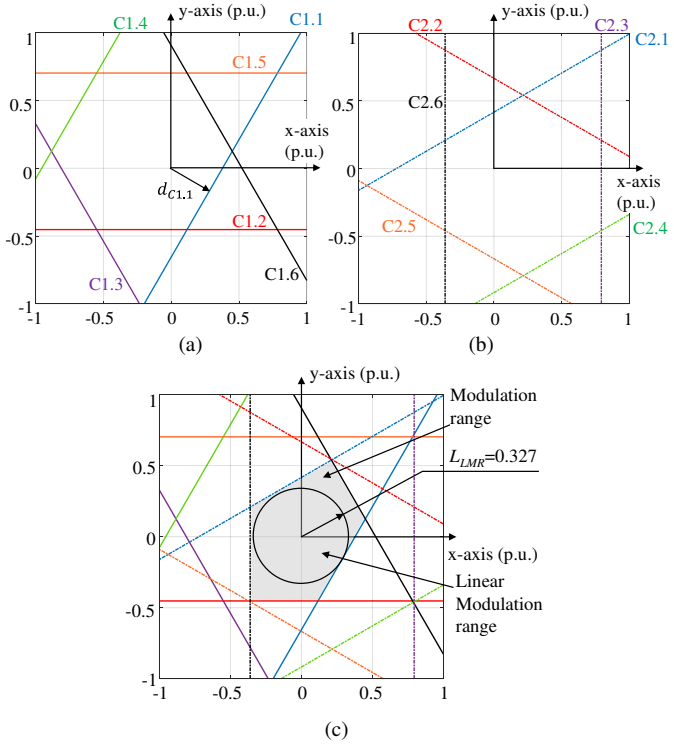

Fig. 5 Linear modulation range in xy subspace for SVPWM-D3 under $\boldsymbol{V^*_{\alpha\beta}} = \left[\frac{\sqrt{3}}{8}V_{dc} \quad \frac{1}{8}V_{dc}\right]^{\mathrm{T}}$. (a) Modulation restrictions regarding Fig. 4(a). (b) Modulation restrictions regarding Fig. 4(b). (c) Linear modulation range of xy subspace combining (a) and (b).

Since the modulation index of the fundamental voltage can generally represent the voltage demand for torque generation and speed control, the linear modulation range under an assured modulation index can be more practical for real applications. Neglecting low-amplitude high-frequency harmonics in αβ subspace, the modulation index of the fundamental voltage in αβ subspace, is defined as

$$m = \frac{\left|\boldsymbol{V^*_{\alpha\beta}}\right|}{\frac{V_{dc}}{2}}. \quad (9)$$

Following the same analysis procedure described in Fig. 5, the magnitude of the linear modulation range under $\boldsymbol{V^*_{\alpha\beta}}$ with the magnitude of $0.25 \cdot V_{dc}$ can be derived and shown in Fig. 6, in which θ_V is the vector angle against α-axis (Fig. 7 (a))

ranging from 0 to 2π. It shows that L_{LMR} varies against θ_V within the range of $0.327 \cdot V_{dc}$ to $0.336 \cdot V_{dc}$. Thus, the minimum value of L_{LMR} with θ_V ranging from 0 to 2π ($L_{LMR} = 0.327 \cdot V_{dc}$) is defined as the magnitude of the linear modulation range under $m = 0.25 \cdot V_{dc}/(0.5 \cdot V_{dc}) = 0.5$. The difference between linear modulation ranges under a specific $\boldsymbol{V^*_{\alpha\beta}}$ and an assured modulation index is explained in Fig. 7. In Fig. 7(a), the modulation of any $\boldsymbol{V^*_{xy}}$ with the magnitude no longer than L_{LMR} would not affect that of the specific $\boldsymbol{V^*_{\alpha\beta}}$. However in Fig. 7(b), the modulation of any $\boldsymbol{V^*_{xy}}$ with the magnitude no longer than L_{LMR} would not affect the modulation of any $\boldsymbol{V^*_{\alpha\beta}}$ with the magnitude of $\frac{V_{dc}}{2} \cdot m$.

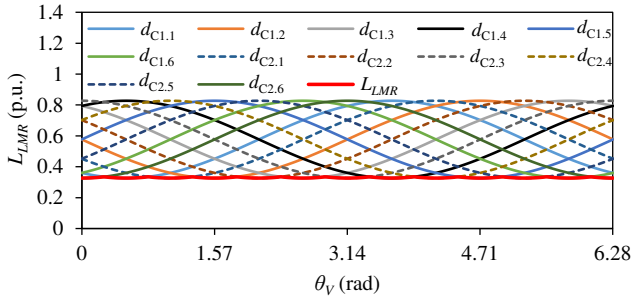

Fig. 6 L_{LMR} against θ_V ranging from 0 to 2π under $|\boldsymbol{V^*_{\alpha\beta}}| = 0.25 \cdot V_{dc}$ for SVPWM-D3.

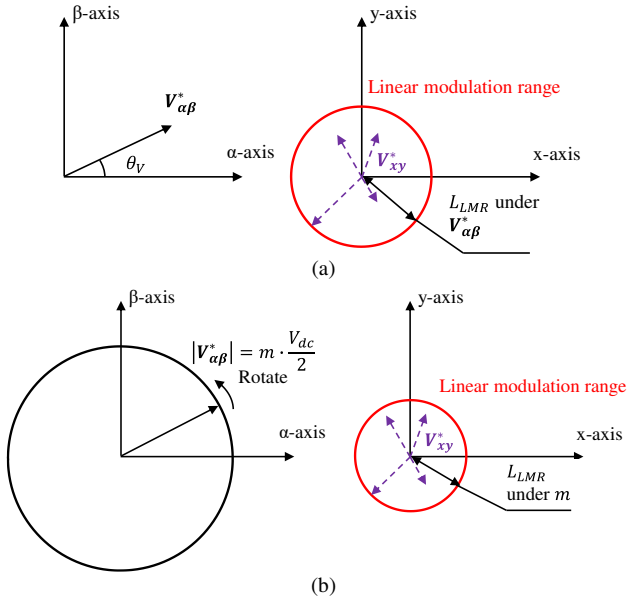

Fig. 7 Schematic diagrams of linear modulation range. (a) Under a specific $\boldsymbol{V^*_{\alpha\beta}}$. (b) Under an assured modulation index.

Till now, the procedures to derive L_{LMR} under the assured modulation index have been explained completely. Follow these procedures, L_{LMR} under the assured modulation index m within the range of $[0, \frac{2}{\sqrt{3}}]$ can be calculated and then plotted in Fig. 8 in which L_{LMR} is scaled with a base of $\frac{V_{dc}}{2}$. It is found from Fig. 8 that L_{LMR} and m are in linear relationship and can be written as

$$L_{LMR} = \frac{V_{dc}}{2} \cdot \left(-m + \frac{2}{\sqrt{3}}\right). \tag{10}$$

From Fig. 8 and (10), there is no linear modulation range under m larger than $\frac{2}{\sqrt{3}}$ for the SVPWM-D3 technique.

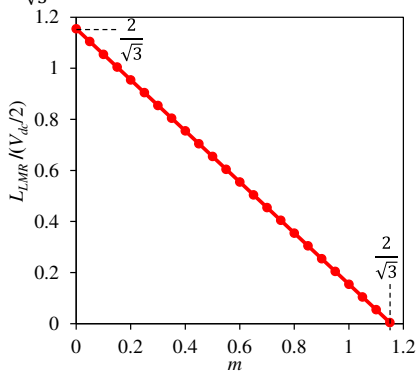

Fig. 8 L_{LMR} under different modulation indices for SVPWM-D3.

B. SVPWM with Four Active Voltage Vectors

The SVPWM technique using four active voltage vectors (SVPWM-4L) [9], [12]-[15] is widely implemented but not researched concerning the modulation restraint. Four active voltage vectors are determined to modulate voltage references during each PWM period. The voltage vector selection principle is presented in Fig. 9. The αβ subspace is divided into 12 sectors using voltage vectors from Dodecagon N_4 as boundaries. The twelve voltage vectors from Dodecagon N_4 in αβ subspace are candidate vectors that can provide a large modulation range in αβ subspace.

In Fig. 9, if $\boldsymbol{V^*_{\alpha\beta}}$ is located between $\boldsymbol{V_{11}}$ and $\boldsymbol{V_9}$ in αβ subspace, four active voltage vectors $\boldsymbol{V_{27}}, \boldsymbol{V_{11}}, \boldsymbol{V_9}$ and $\boldsymbol{V_{41}}$ are selected to modulate $\boldsymbol{V^*_{\alpha\beta}}$ and $\boldsymbol{V^*_{xy}}$ in two subspaces, respectively. In such a case, twelve sectors and four active voltage vectors determined by the location of $\boldsymbol{V^*_{\alpha\beta}}$ are shown in Table I.

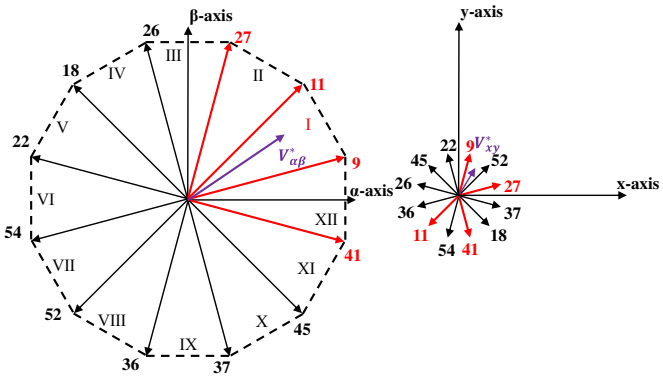

Fig. 9 Sector division and voltage vector selection principle for SVPWM-4L. (a) αβ subspace. (b) xy subspace.

The modulation procedure is described in (11) and zero voltage vectors are applied to fill in the gap of each PWM period.

$$\begin{bmatrix} T_{SA} \\ T_{SB} \\ T_{SC} \\ T_{SD} \end{bmatrix} = T_{PWM} \begin{bmatrix} V_{SA\alpha} & V_{SB\alpha} & V_{SC\alpha} & V_{SD\alpha} \\ V_{SA\beta} & V_{SB\beta} & V_{SC\beta} & V_{SD\beta} \\ V_{SAx} & V_{SBx} & V_{SCx} & V_{SDx} \\ V_{SAy} & V_{SBy} & V_{SCy} & V_{SDy} \end{bmatrix}^{-1} \begin{bmatrix} u_\alpha^* \\ u_\beta^* \\ u_x^* \\ u_y^* \end{bmatrix}, \quad (11)$$

in which, $V_{SA\alpha}$, $V_{SB\alpha}$, $V_{SC\alpha}$, $V_{SD\alpha}$ denote projections of $\boldsymbol{V_{SA}}$, $\boldsymbol{V_{SB}}$, $\boldsymbol{V_{SC}}$, $\boldsymbol{V_{SD}}$ on α-axis. For projections on β-axis, x-axis, and y-axis, similar denotations apply. T_{SA}, T_{SB}, T_{SC} and T_{SD} denote dwell times of $\boldsymbol{V_{SA}}$, $\boldsymbol{V_{SB}}$, $\boldsymbol{V_{SC}}$, $\boldsymbol{V_{SD}}$, respectively.

TABLE I
SECTOR DIVISION AND VOLTAGE VECTOR SELECTION FOR SVPWM-4L

Sector	$\boldsymbol{V_{SA}}$	$\boldsymbol{V_{SB}}$	$\boldsymbol{V_{SC}}$	$\boldsymbol{V_{SD}}$
I	27	11	9	41
II	26	27	11	9
III	18	26	27	11
IV	22	18	26	27
V	54	22	18	26
VI	52	54	22	18
VII	36	52	54	22
VIII	37	36	52	54
IX	45	37	36	52
X	41	45	37	36
XI	9	41	45	37
XII	11	9	41	45

However, it cannot ensure there is always a solution to (11). Dwell times have restrictions shown in (12) which should be satisfied and T_Z is the dwell time of zero voltage vectors.

$$\begin{cases} T_{SA} \geq 0 \\ T_{SB} \geq 0 \\ T_{SC} \geq 0 \\ T_{SD} \geq 0 \\ T_z = T_{PWM} - (T_{SA} + T_{SB} + T_{SC} + T_{SD}) \geq 0 \end{cases} \quad (12)$$

Substitute (11) into (12), the modulation range of xy subspace related to u_α^* and u_β^* can be derived. Similarly, $\boldsymbol{V_{\alpha\beta}^*} = \left[\frac{\sqrt{3}}{8}V_{dc} \quad \frac{1}{8}V_{dc}\right]^{\mathrm{T}}$ is set as an example and $\boldsymbol{V_{27}}, \boldsymbol{V_{11}}, \boldsymbol{V_9}$ and $\boldsymbol{V_{41}}$ are selected under this case. Then, the modulation range of xy subspace is shown in Fig. 10 in the per-unit scale with respect to V_{dc}. From Fig. 10, each line presents one dwell time restriction in (12). The shadowed area is the modulation range of xy subspace under $\boldsymbol{V_{\alpha\beta}^*} = \left[\frac{\sqrt{3}}{8}V_{dc} \quad \frac{1}{8}V_{dc}\right]^{\mathrm{T}}$. The distances from the point of origin to lines of T_{SA}, T_{SB}, T_{SC}, T_{SD} and T_Z in (12), are denoted as d_{SA}, d_{SB}, d_{SC}, d_{SD} and d_Z. The distance d_{SA} is presented in Fig. 10 as an example. Similarly, the circle indicates the linear modulation range and the magnitude (L_{LMR}), i.e. the radius, is the minimum value among d_{SA}, d_{SB}, d_{SC}, d_{SD} and d_Z, which is $L_{LMR} = \mathrm{Min}\{d_{SA}, d_{SB}, d_{SC}, d_{SD}, d_Z\} = 0.017 \cdot V_{dc}$ under this case.

Then, the linear modulation range of xy subspace under $\boldsymbol{V_{\alpha\beta}^*}$ with the magnitude of $0.25 \cdot V_{dc}$ and vector angle ranging from 0 to 2π can be derived, shown in Fig. 11. From Fig. 11, L_{LMR} is relatively small and varies from 0 to $0.017 \cdot V_{dc}$. Thus, the linear modulation range under $m = 0.5$ has the magnitude of $L_{LMR} = 0$ for SVPWM-4L. Moreover, the magnitude of the linear modulation range under $m \in [0, \frac{2}{\sqrt{3}}]$ is analyzed to be zero.

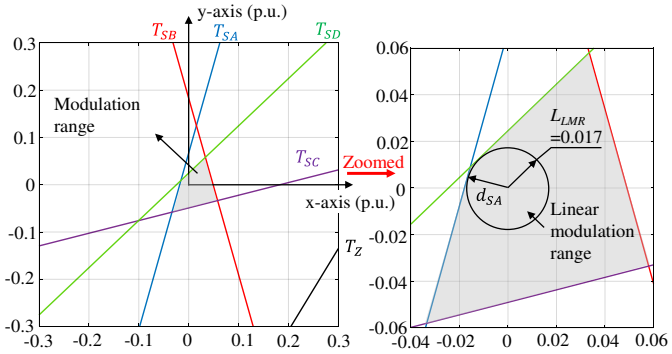

Fig. 10 Modulation range in xy subspace for SVPWM-4L under $\boldsymbol{V_{\alpha\beta}^*} = \left[\frac{\sqrt{3}}{8}V_{dc} \quad \frac{1}{8}V_{dc}\right]^{\mathrm{T}}$.

C. Enhanced SVPWM with Synthetic Vectors

Synthetic vectors composed of two voltage vectors can be implemented to achieve a decoupled modulation of voltage references in two subspaces indirectly [20]. In this SVPWM technique [20], the modulations in two subspaces do not affect each other.

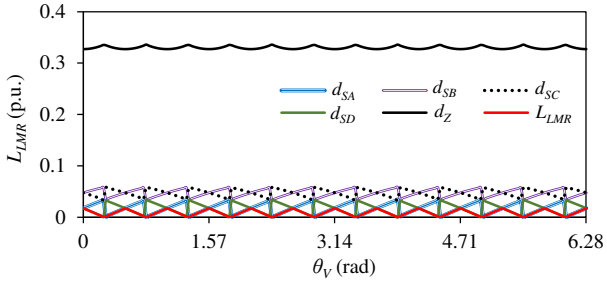

Fig. 11 L_{LMR} against θ_V ranging from 0 to 2π under $|\boldsymbol{V_{\alpha\beta}^*}| = 0.25 \cdot V_{dc}$ for SVPWM-4L.

The enhanced SVPWM with synthetic vectors (SVPWM-SV) is further developed from [20] with optimization of sector division and switching pattern generation. In SVPWM-SV [20], each PWM period T_{PWM} is split into two parts, denoted as $T_{\alpha\beta}$ and T_{xy} which are calculated according to the lengths of $\boldsymbol{V_{\alpha\beta}^*}$ and $\boldsymbol{V_{xy}^*}$, shown as

$$\begin{cases} T_{\alpha\beta} = \dfrac{|\boldsymbol{V_{\alpha\beta}^*}|}{|\boldsymbol{V_{\alpha\beta}^*}| + |\boldsymbol{V_{xy}^*}|} \cdot T_{PWM} \\ T_{xy} = \dfrac{|\boldsymbol{V_{xy}^*}|}{|\boldsymbol{V_{\alpha\beta}^*}| + |\boldsymbol{V_{xy}^*}|} \cdot T_{PWM} \end{cases}. \quad (13)$$

In the period of $T_{\alpha\beta}$, $\boldsymbol{V_{\alpha\beta}^*}$ is modulated through two synthetic vectors and the average zero voltage in xy subspace is achieved, as shown in Fig. 12, where $\boldsymbol{V_{\alpha\beta}^*}$ locates at Sector I and synthetic vectors $\boldsymbol{V_{SV1}}$, $\boldsymbol{V_{SV2}}$ are formed by $\boldsymbol{V_{11}}$, $\boldsymbol{V_{25}}$ and $\boldsymbol{V_9}$, $\boldsymbol{V_{43}}$, respectively, used to modulate $\boldsymbol{V_{\alpha\beta}^*}$. The sector division is the same as SVPWM-4L. Following the same rule, the synthetic vectors implemented for $\boldsymbol{V_{\alpha\beta}^*}$ locating at all sectors are presented in Table II, in which $\boldsymbol{V_{SA\_\alpha\beta}}$, $\boldsymbol{V_{SC\_\alpha\beta}}$ are N_4 voltage

vectors and $\boldsymbol{V_{SB\_\alpha\beta}}$, $\boldsymbol{V_{SD\_\alpha\beta}}$ are N_3 voltage vectors in αβ subspace.

Then, the procedure to obtain the synthetic vectors is illustrated. It can be seen that $\boldsymbol{V_{SA\_\alpha\beta}}$ and $\boldsymbol{V_{SB\_\alpha\beta}}$ ($\boldsymbol{V_{SC\_\alpha\beta}}$ and $\boldsymbol{V_{SD\_\alpha\beta}}$) are in phase in αβ subspace, but are out of phase in xy subspace. Therefore, through the proposed allocation of dwell times, the average zero voltage in xy subspace is achieved by

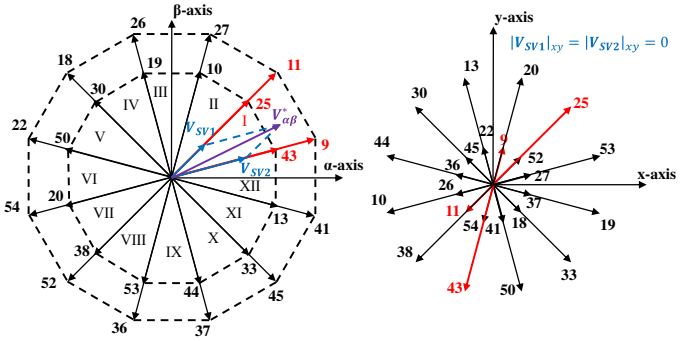

Fig. 12 Sector division and synthetic vector composition in αβ subspace for SVPWM-SV. (a) αβ subspace. (b) xy subspace.

TABLE II
SECTOR DIVISION AND VOLTAGE VECTOR SELECTION FOR SYNTHETIC VECTORS IN αβ SUBSPACE

Sector	$\boldsymbol{V_{SV1}}$		$\boldsymbol{V_{SV2}}$	
	$\boldsymbol{V_{SA\_\alpha\beta}}$	$\boldsymbol{V_{SB\_\alpha\beta}}$	$\boldsymbol{V_{SC\_\alpha\beta}}$	$\boldsymbol{V_{SD\_\alpha\beta}}$
I	11	25	9	43
II	27	10	11	25
III	26	19	27	10
IV	18	30	26	19
V	22	50	18	30
VI	54	20	22	50
VII	52	38	54	20
VIII	36	53	52	38
IX	37	44	36	53
X	45	33	37	44
XI	41	13	45	33
XII	9	43	41	13

$$\begin{cases} L_{N3}\cdot T_{SB\_\alpha\beta} - L_{N1}\cdot T_{SA\_\alpha\beta} = 0 \\ T_{SA\_\alpha\beta} + T_{SB\_\alpha\beta} = T_{SV1} \end{cases}, \tag{14}$$

$$\begin{cases} L_{N3}\cdot T_{SD\_\alpha\beta} - L_{N1}\cdot T_{SC\_\alpha\beta} = 0 \\ T_{SC\_\alpha\beta} + T_{SD\_\alpha\beta} = T_{SV2} \end{cases}, \tag{15}$$

in which, $T_{SA\_\alpha\beta}$, $T_{SB\_\alpha\beta}$, $T_{SC\_\alpha\beta}$ and $T_{SD\_\alpha\beta}$ denote dwell times of $\boldsymbol{V_{SA\_\alpha\beta}}$, $\boldsymbol{V_{SB\_\alpha\beta}}$, $\boldsymbol{V_{SC\_\alpha\beta}}$ and $\boldsymbol{V_{SD\_\alpha\beta}}$, respectively; L_{N1}, L_{N3} are shown in (4); T_{SV1} and T_{SV2} denote dwell times of $\boldsymbol{V_{SV1}}$ and $\boldsymbol{V_{SV2}}$, respectively. Then, $T_{SA\_\alpha\beta}$, $T_{SB\_\alpha\beta}$, $T_{SC\_\alpha\beta}$ and $T_{SD\_\alpha\beta}$ calculated from (14) and (15) can be expressed as

$$\begin{cases} T_{SA\_\alpha\beta} = \dfrac{2\sqrt{2}}{\sqrt{6}+\sqrt{2}}\cdot T_{SV1} \\ T_{SB\_\alpha\beta} = \dfrac{\sqrt{6}-\sqrt{2}}{\sqrt{6}+\sqrt{2}}\cdot T_{SV1} \end{cases}, \tag{16}$$

$$\begin{cases} T_{SC\_\alpha\beta} = \dfrac{2\sqrt{2}}{\sqrt{6}+\sqrt{2}}\cdot T_{SV2} \\ T_{SD\_\alpha\beta} = \dfrac{\sqrt{6}-\sqrt{2}}{\sqrt{6}+\sqrt{2}}\cdot T_{SV2} \end{cases}. \tag{17}$$

According to (16) and (17), the length of the synthetic vectors $\boldsymbol{V_{SV1}}$ and $\boldsymbol{V_{SV2}}$ in αβ and xy subspaces can be expressed as

$$\begin{cases} |\boldsymbol{V_{SV1}}|_{\alpha\beta} = \dfrac{L_{N4}\cdot T_{SA\_\alpha\beta} + L_{N3}\cdot T_{SB\_\alpha\beta}}{T_{PWM}} \\ \qquad\qquad = \dfrac{3\sqrt{2}-\sqrt{6}}{3}\cdot V_{dc}\cdot\dfrac{T_{SV1}}{T_{PWM}} \\ |\boldsymbol{V_{SV1}}|_{xy} = 0 \end{cases}, \tag{18}$$

$$\begin{cases} |\boldsymbol{V_{SV2}}|_{\alpha\beta} = \dfrac{L_{N4}\cdot T_{SC\_\alpha\beta} + L_{N3}\cdot T_{SD\_\alpha\beta}}{T_{PWM}} \\ \qquad\qquad = \dfrac{3\sqrt{2}-\sqrt{6}}{3}\cdot V_{dc}\cdot\dfrac{T_{SV2}}{T_{PWM}} \\ |\boldsymbol{V_{SV2}}|_{xy} = 0 \end{cases}, \tag{19}$$

where $|\boldsymbol{V_{SV1}}|_{\alpha\beta}$ and $|\boldsymbol{V_{SV1}}|_{xy}$ denotes the lengths of $\boldsymbol{V_{SV1}}$ in αβ and xy subspaces, respectively; $|\boldsymbol{V_{SV2}}|_{\alpha\beta}$ and $|\boldsymbol{V_{SV2}}|_{xy}$ denotes the lengths of $\boldsymbol{V_{SV2}}$ in αβ and xy subspaces, respectively. Then, substituting (18) and (19) into (16) and (17), respectively, (16) and (17) can be rewritten as

$$\begin{bmatrix} T_{SA\_\alpha\beta} \\ T_{SB\_\alpha\beta} \\ T_{SC\_\alpha\beta} \\ T_{SD\_\alpha\beta} \end{bmatrix} = \frac{T_{PWM}}{V_{dc}}\cdot\begin{bmatrix} \dfrac{\sqrt{6}}{2} & 0 \\ \dfrac{\sqrt{3}}{\sqrt{6}+\sqrt{2}} & 0 \\ 0 & \dfrac{\sqrt{6}}{2} \\ 0 & \dfrac{\sqrt{3}}{\sqrt{6}+\sqrt{2}} \end{bmatrix}\begin{bmatrix} |\boldsymbol{V_{SV1}}|_{\alpha\beta} \\ |\boldsymbol{V_{SV2}}|_{\alpha\beta} \end{bmatrix}. \tag{20}$$

Of note, the synthetic vector $\boldsymbol{V_{SV1}}$ is in phase with $\boldsymbol{V_{SA\_\alpha\beta}}$ and $\boldsymbol{V_{SB\_\alpha\beta}}$ in αβ subspace. Similarly, the synthetic vector $\boldsymbol{V_{SV2}}$ is in phase with $\boldsymbol{V_{SC\_\alpha\beta}}$ and $\boldsymbol{V_{SD\_\alpha\beta}}$ in αβ subspace as well. From (18) and (19), the average zero voltage in xy subspace will be maintained when $\boldsymbol{V_{SV1}}$ and $\boldsymbol{V_{SV2}}$ are used to modulate $\boldsymbol{V^*_{\alpha\beta}}$. Then, the modulation of $\boldsymbol{V^*_{\alpha\beta}}$.can be described as

$$\begin{bmatrix} |\boldsymbol{V_{SV1}}|_{\alpha\beta} \\ |\boldsymbol{V_{SV2}}|_{\alpha\beta} \end{bmatrix} = \begin{bmatrix} \cos\left(\mu+\dfrac{\pi}{6}\right) & \cos(\mu) \\ \sin\left(\mu+\dfrac{\pi}{6}\right) & \sin(\mu) \end{bmatrix}^{-1}\begin{bmatrix} u^*_\alpha \\ u^*_\beta \end{bmatrix}, \tag{21}$$

in which, $\mu = \frac{\pi}{6}\cdot n - \frac{\pi}{12}$ $(n = 1,2,\ldots,12)$. n is corresponding to the sector number in αβ subspace and for example, if $\boldsymbol{V^*_{\alpha\beta}}$ is in Sector I, n =1. Then, substituting (21) into (20), the dwell times of voltage vectors in the first part $T_{\alpha\beta}$ can be obtained according to $\boldsymbol{V^*_{\alpha\beta}}$. Meanwhile, the dwell times of zero voltage vectors can be calculated as

$$T_{0\_\alpha\beta} = T_{63\_\alpha\beta} = \frac{T_{\alpha\beta} - T_{SA\_\alpha\beta} - T_{SB\_\alpha\beta} - T_{SC\_\alpha\beta} - T_{SD\_\alpha\beta}}{2}, \quad (22)$$

where $T_{0\_\alpha\beta}$ and $T_{63\_\alpha\beta}$ denote the dwell times of $\boldsymbol{V_0}$ and $\boldsymbol{V_{63}}$ in the period of $T_{\alpha\beta}$, respectively.

In the period of T_{xy}, $\boldsymbol{V_{xy}^*}$ is modulated through two synthetic vectors and the average zero voltage in αβ subspace is maintained, as shown in Fig. 13, where $\boldsymbol{V_{xy}^*}$ locates at Sector I and two synthetic vectors $\boldsymbol{V_{SV3}}$, $\boldsymbol{V_{SV4}}$ formed by $\boldsymbol{V_{21}}$, $\boldsymbol{V_{25}}$ and $\boldsymbol{V_{17}}$, $\boldsymbol{V_{53}}$, respectively, used to modulate $\boldsymbol{V_{xy}^*}$. Following the same rule, the synthetic vectors implemented for $\boldsymbol{V_{xy}^*}$ locating at all sectors are presented in Table III, in which $\boldsymbol{V_{SA\_xy}}$, $\boldsymbol{V_{SC\_xy}}$ are N_4 voltage vectors and $\boldsymbol{V_{SB\_xy}}$, $\boldsymbol{V_{SD\_xy}}$ are N_3 voltage vectors in xy subspace. The procedures to obtain the length of $\boldsymbol{V_{SV3}}$, $\boldsymbol{V_{SV4}}$ in xy subspace and their dwell times are the same as those for $\boldsymbol{V_{SV1}}$, $\boldsymbol{V_{SV2}}$ in αβ subspace shown in (14)-(19), but are conducted in xy subspace. Then, the lengths of $\boldsymbol{V_{SV3}}$ and $\boldsymbol{V_{SV4}}$ are shown as

$$\begin{cases} |\boldsymbol{V_{SV3}}|_{\alpha\beta} = 0 \\ |\boldsymbol{V_{SV3}}|_{xy} = \dfrac{3\sqrt{2}-\sqrt{6}}{3} \cdot V_{dc} \cdot \dfrac{T_{SV3}}{T_{PWM}} \end{cases}, \quad (23)$$

$$\begin{cases} |\boldsymbol{V_{SV4}}|_{\alpha\beta} = 0 \\ |\boldsymbol{V_{SV4}}|_{xy} = \dfrac{3\sqrt{2}-\sqrt{6}}{3} \cdot V_{dc} \cdot \dfrac{T_{SV4}}{T_{PWM}} \end{cases}, \quad (24)$$

in which, $|\boldsymbol{V_{SV3}}|_{xy}$ and $|\boldsymbol{V_{SV4}}|_{xy}$ denote the lengths of $\boldsymbol{V_{SV3}}$ and $\boldsymbol{V_{SV4}}$ in xy subspace, respectively; $|\boldsymbol{V_{SV3}}|_{\alpha\beta}$ and $|\boldsymbol{V_{SV4}}|_{\alpha\beta}$ denote the lengths of $\boldsymbol{V_{SV3}}$ and $\boldsymbol{V_{SV4}}$ in αβ subspace, respectively, which are zero; T_{SV3} and T_{SV4} denote the dwell times of $\boldsymbol{V_{SV3}}$ and $\boldsymbol{V_{SV4}}$, respectively.

Similarly, the modulation of $\boldsymbol{V_{xy}^*}$ can be described as

$$\begin{bmatrix} |\boldsymbol{V_{SV3}}|_{xy} \\ |\boldsymbol{V_{SV4}}|_{xy} \end{bmatrix} = \begin{bmatrix} \cos\left(\sigma + \dfrac{\pi}{6}\right) & \cos(\sigma) \\ \sin\left(\sigma + \dfrac{\pi}{6}\right) & \sin(\sigma) \end{bmatrix}^{-1} \begin{bmatrix} u_x^* \\ u_y^* \end{bmatrix}, \quad (25)$$

in which; $\sigma = \frac{\pi}{6} \cdot q - \frac{\pi}{12}$ $(q = 1,2,\ldots,12)$. q is corresponding to the sector number in xy subspace and for example, if $\boldsymbol{V_{xy}^*}$ is in Sector I, q =1. Similarly, the dwell times of voltage vectors in the period of T_{xy} can be expressed as

$$\begin{bmatrix} T_{SA\_xy} \\ T_{SB\_xy} \\ T_{SC\_xy} \\ T_{SD\_xy} \end{bmatrix} = \frac{T_{PWM}}{V_{dc}} \cdot \begin{bmatrix} \dfrac{\sqrt{6}}{2} & 0 \\ \dfrac{\sqrt{3}}{\sqrt{6}+\sqrt{2}} & 0 \\ 0 & \dfrac{\sqrt{6}}{2} \\ 0 & \dfrac{\sqrt{3}}{\sqrt{6}+\sqrt{2}} \end{bmatrix} \begin{bmatrix} |\boldsymbol{V_{SV3}}|_{xy} \\ |\boldsymbol{V_{SV4}}|_{xy} \end{bmatrix}, \quad (26)$$

$$T_{0\_xy} = T_{63\_xy} = \frac{T_{xy} - T_{SA\_xy} - T_{SB\_xy} - T_{SC\_xy} - T_{SD\_xy}}{2} \quad (27)$$

where T_{SA_xy}, T_{SB_xy}, T_{SC_xy} and T_{SD_xy} denote the dwell times of $\boldsymbol{V_{SA\_xy}}$, $\boldsymbol{V_{SB\_xy}}$, $\boldsymbol{V_{SC\_xy}}$ and $\boldsymbol{V_{SD\_xy}}$, respectively; T_{0_xy} and T_{63_xy} denote the dwell times of $\boldsymbol{V_0}$ and $\boldsymbol{V_{63}}$ in the period of T_{xy}, respectively.

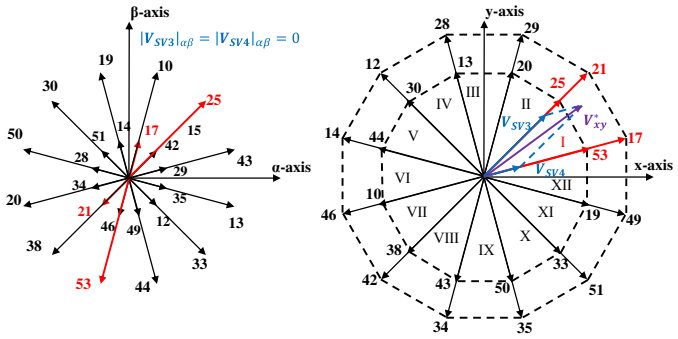

(a) (b)

Fig. 13 Sector division and synthetic vector composition in xy subspace for SVPWM-SV. (a) αβ subspace. (b) xy subspace.

TABLE III
SECTOR DIVISION AND VOLTAGE VECTOR SELECTION FOR SYNTHETIC VECTORS IN xy SUBSPACE

Sector	$\boldsymbol{V_{SV3}}$		$\boldsymbol{V_{SV4}}$	
	$\boldsymbol{V_{SA\_xy}}$	$\boldsymbol{V_{SB\_xy}}$	$\boldsymbol{V_{SC\_xy}}$	$\boldsymbol{V_{SD\_xy}}$
I	21	25	17	53
II	29	20	21	25
III	28	13	29	20
IV	12	30	28	13
V	14	44	12	30
VI	46	10	14	44
VII	42	38	46	10
VIII	34	43	42	38
IX	35	50	34	43
X	51	33	35	50
XI	49	19	51	33
XII	17	53	49	19

Then the final step is to arrange the switching sequence according to dwell times calculated as (20), (22), (26), and (27). For instance, the switching sequence for $\boldsymbol{V_{\alpha\beta}^*} = \begin{bmatrix} \frac{\sqrt{3}}{8}V_{dc} & \frac{1}{8}V_{dc} \end{bmatrix}^{\mathrm{T}}$ and $\boldsymbol{V_{xy}^*} = \begin{bmatrix} \frac{\sqrt{3}}{16}V_{dc} & \frac{1}{16}V_{dc} \end{bmatrix}^{\mathrm{T}}$ are presented in Fig. 14.

The flowchart of the SVPWM-SV technique can be summarized in Fig. 15. The PWM period split makes the SVPWM-SV technique complicated. On the other hand, it can be seen from Fig. 14 that phases experience multiple switching during each PWM period leading to high switching loss. Meanwhile, the complicated switching sequence arrangement with too many voltage vectors poses a significant challenge for microcontrollers. Therefore, the SVPWM-SV in [20] can be improved to become more practical and accessible.

In the enhanced SVPWM-SV technique, there is no PWM period split and the modulations of $\boldsymbol{V_{\alpha\beta}^*}$ and $\boldsymbol{V_{xy}^*}$ are firstly achieved by using (21) and (25). Then, the dwell times of $\boldsymbol{V_{SA\_\alpha\beta}}$, $\boldsymbol{V_{SB\_\alpha\beta}}$, $\boldsymbol{V_{SC\_\alpha\beta}}$, $\boldsymbol{V_{SD\_\alpha\beta}}$, $\boldsymbol{V_{SA\_xy}}$, $\boldsymbol{V_{SB\_xy}}$, $\boldsymbol{V_{SC\_xy}}$ and

$\boldsymbol{V_{SD\_xy}}$ can be calculated according to (20) and (26). The dwell times of zero voltage vectors $\boldsymbol{V_0}$ and $\boldsymbol{V_{63}}$, denoted by T_0 and T_{63}, respectively in the period of T_{PWM} can be expressed as

$$T_0 = T_{63} = \frac{T_{PWM}}{2} - \frac{T_{SA\_\alpha\beta} + T_{SB\_\alpha\beta} + T_{SC\_\alpha\beta} + T_{SD\_\alpha\beta}}{2} - \frac{T_{SA\_xy} + T_{SB\_xy} + T_{SC\_xy} + T_{SD\_xy}}{2} \quad (28)$$

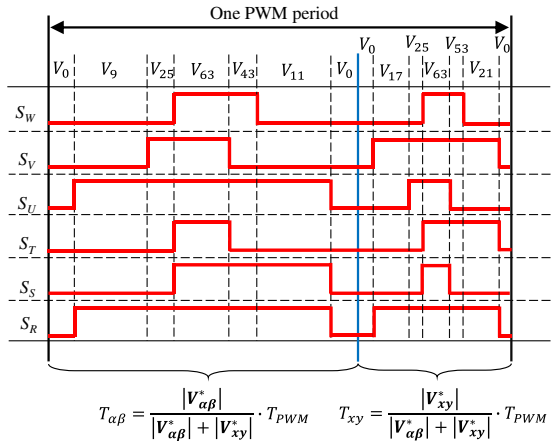

Fig. 14 PWM period split and switching sequence generation for $\boldsymbol{V^*_{\alpha\beta}} = \left[\frac{\sqrt{3}}{8}V_{dc} \quad \frac{1}{8}V_{dc}\right]^{\mathrm{T}}$ and $\boldsymbol{V^*_{xy}} = \left[\frac{\sqrt{3}}{16}V_{dc} \quad \frac{1}{16}V_{dc}\right]^{\mathrm{T}}$ in SVPWM-SV [20].

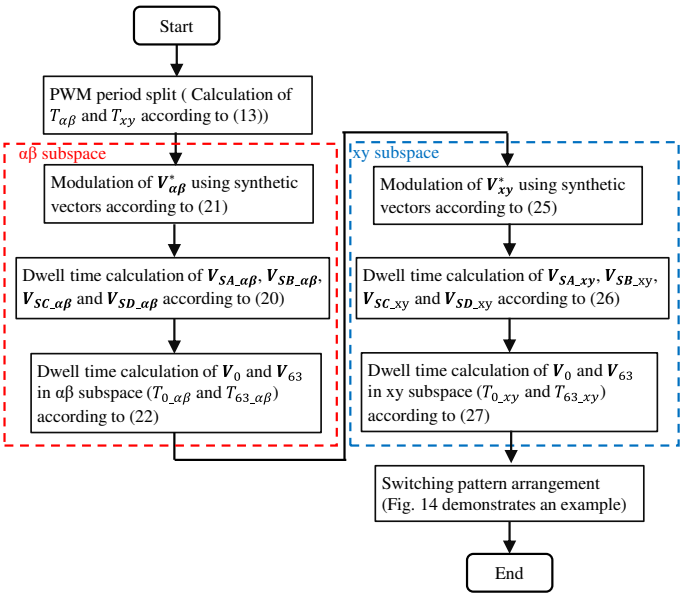

Fig. 15 Flowchart of SVPWM-SV [20].

The next step is to calculate the duty cycle of each phase according to (20), (26), and (28). Still using the example $\boldsymbol{V^*_{\alpha\beta}} = \left[\frac{\sqrt{3}}{8}V_{dc} \quad \frac{1}{8}V_{dc}\right]^{\mathrm{T}}$ and $\boldsymbol{V^*_{xy}} = \left[\frac{\sqrt{3}}{16}V_{dc} \quad \frac{1}{16}V_{dc}\right]^{\mathrm{T}}$, duty cycles of phases can be calculated as (29). Then, the switching sequence is generated from (29) and the turn-on time of each phase is allocated in the middle of the switching pattern, as shown in Fig. 16. There will be no multiple switching in each phase and no complicated switching sequence arrangement, compared with the SVPWM-SV in [20] shown as Fig. 14. Of note, the switch sequence in Fig. 14 and Fig. 16 are different, but both of them can modulate $\boldsymbol{V^*_{\alpha\beta}} = \left[\frac{\sqrt{3}}{8}V_{dc} \quad \frac{1}{8}V_{dc}\right]^{\mathrm{T}}$ and $\boldsymbol{V^*_{xy}} = \left[\frac{\sqrt{3}}{16}V_{dc} \quad \frac{1}{16}V_{dc}\right]^{\mathrm{T}}$. Additionally, the generation of the switching sequence in in Fig. 16 is much simpler for microcontrollers.

$$\begin{cases} D_R = \dfrac{T_{PWM} - T_0}{T_{PWM}} \\ D_S = \dfrac{T_{SA\_\alpha\beta} + T_{SD\_\alpha\beta} + T_{63}}{T_{PWM}} \\ D_T = \dfrac{T_{SA\_xy} + T_{SD\_xy} + T_{63}}{T_{PWM}} \\ D_U = \dfrac{T_{SA\_\alpha\beta} + T_{SB\_\alpha\beta} + T_{SC\_\alpha\beta} + T_{SD\_\alpha\beta} + T_{SB\_xy} + T_{63}}{T_{PWM}} \\ D_V = \dfrac{T_{SA\_xy} + T_{SB\_xy} + T_{SC\_xy} + T_{SD\_xy} + T_{SB\_\alpha\beta} + T_{63}}{T_{PWM}} \\ D_W = \dfrac{T_{SD\_\alpha\beta} + T_{SD\_xy} + T_{63}}{T_{PWM}} \end{cases} \quad (29)$$

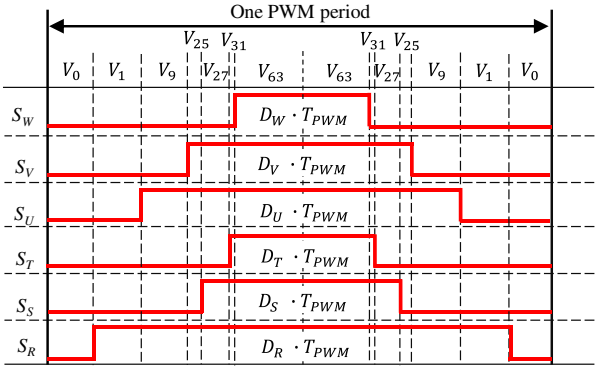

Fig. 16 Switching sequence generated from (29) for $\boldsymbol{V^*_{\alpha\beta}} = \left[\frac{\sqrt{3}}{8}V_{dc} \quad \frac{1}{8}V_{dc}\right]^{\mathrm{T}}$ and $\boldsymbol{V^*_{xy}} = \left[\frac{\sqrt{3}}{16}V_{dc} \quad \frac{1}{16}V_{dc}\right]^{\mathrm{T}}$ in enhanced SVPWM-SV.

The steps of the enhanced SVPWM-SV technique can be summarized in Fig. 17. Comparing Fig. 15 and Fig. 17, the steps of the enhanced SVPWM-SV technique are simpler. The outstanding benefits are no PWM period split and no multiple switching per phase.

Since the enhanced SVPWM-SV can modulate voltage references in αβ and xy subspaces separately without being coupled by dwell times of voltage vectors, the derivation of linear modulation range is more straightforward than SVPWM-4L and SVPWM-D3. The modulation in αβ subspace (Sector I as an example) can be described as Fig. 18, in which γ is the angle between $\boldsymbol{V^*_{\alpha\beta}}$ and $\boldsymbol{V_{SV2}}$. Then, T_{SV1} and T_{SV2} against m can be derived using (30).

$$\frac{|\boldsymbol{V^*_{\alpha\beta}}|}{\sin\left(\frac{5}{6}\pi\right)} = \frac{|\boldsymbol{V_{SV1}}|_{\alpha\beta}}{\sin(\gamma)} = \frac{|\boldsymbol{V_{SV2}}|_{\alpha\beta}}{\sin\left(\frac{1}{6}\pi - \gamma\right)}. \quad (30)$$

Substituting (9), (18), (19) into (30), $T_{SV1} + T_{SV2}$ reflecting the period consumed to modulate $\boldsymbol{V^*_{\alpha\beta}}$ in one PWM period can be expressed as

$$T_{SV1}+T_{SV2}=\frac{3T_{PWM}\cdot m}{3\sqrt{2}-\sqrt{6}}\cdot\left(\sin(\gamma)+\sin\left(\frac{1}{6}\pi-\gamma\right)\right), \quad (31)$$

in which $\gamma\in\left[0,\frac{1}{6}\pi\right]$. Then, the maximum value of (31) is $\frac{\sqrt{3}}{2}T_{PWM}\cdot m$. Since the modulations of αβ and xy subspaces are decoupled, following the same procedure, the maximum value of $T_{SV3}+T_{SV4}$ is $\frac{\sqrt{3}}{2}T_{PWM}\cdot\frac{|\boldsymbol{V}_{xy}^{*}|}{\frac{V_{dc}}{2}}$. Due to the restriction of dwell times, $T_{SV1}+T_{SV2}+T_{SV3}+T_{SV4}\le T_{PWM}$, L_{LMR} can be expressed as

$$L_{LMR}=\frac{V_{dc}}{2}\cdot\left(-m+\frac{2}{\sqrt{3}}\right). \quad (32)$$

It can be seen from (10) and (32) that SVPWM-D3 and the enhanced SVPWM-SV have the same modulation restraint.

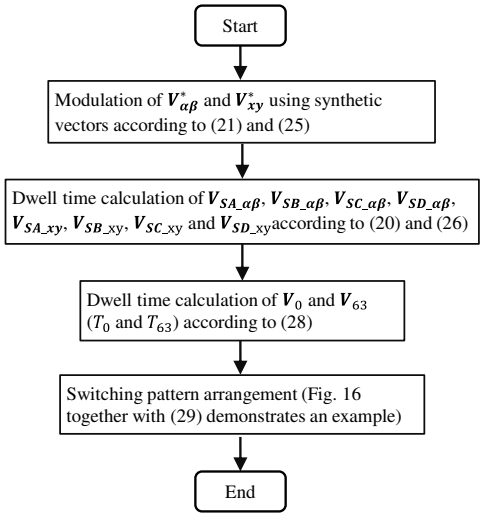

Fig. 17 Flowchart of enhanced SVPWM-SV.

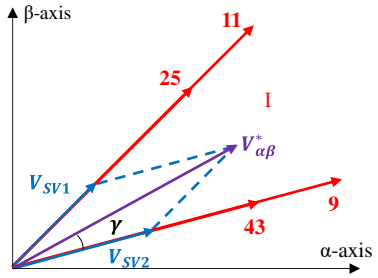

Fig. 18 Modulation in αβ subspace for enhanced SVPWM-SV (Sector I as an example).

D. Summary

The plot of L_{LMR} under m for SVPWM-D3, SVPWM-4L and the enhanced SVPWM-SV can be summarized in Fig. 19(a). It should be noted that there is no linear modulation range in xy subspace under m larger than $\frac{2}{\sqrt{3}}$ for all SVPWM techniques. For SVPWM-4L, L_{LMR} is zero under all modulation indices, while L_{LMR} against m is the same for SVPWM-D3 and the enhanced SVPWM-SV. The schematic diagram of the linear modulation range of SVPWM-D3 and the enhanced SVPWM-SV presented in xy subspace is shown in Fig. 19(b). The magnitude of the linear modulation range reaches $\frac{V_{dc}}{\sqrt{3}}$ (max) under $m=0$ and it shrinks to zero under $m=\frac{2}{\sqrt{3}}$.

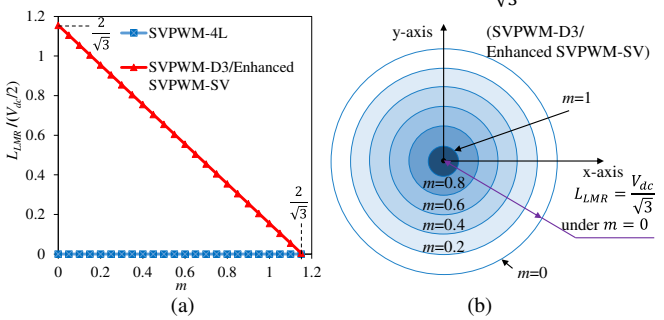

Fig. 19 Linear modulation range comparison. (a) L_{LMR} under different modulation indices. (b) Schematic diagram of linear modulation range in xy subspace for SVPWM-D3 and enhanced SVPWM-SV.

Since the value of m can be estimated through the torque requirement or fundamental current amplitude under the operation speed, the linear modulation range of SVPWM-D3 and the enhanced SVPWM-SV can be derived from (1), (2), (9), and (32) under such working conditions to ensure the control of xy subspace would not affect the current control in αβ subspace. An example of the linear modulation range derivation under a given fundamental current is illustrated in Section IV.

However, there are some restrictions in this modulation restraint analysis. Firstly, only fundamental voltage modulation reflected by the modulation index is considered in αβ subspace, however the $12k\pm1$ (k=1,2,3⋯) order harmonics with much small amplitudes are neglected. If their amplitudes are large enough to consider (normally rare), the linear modulation range in xy subspace will shrink. Secondly, there is an achievable nonlinear modulation range in xy subspace in each PWM period in addition to the calculated linear modulation range under the correspondence modulation index. For example, the shadowed area in Fig. 5(c) is the total modulation range including the nonlinear modulation range. However, the nonlinear modulation range will generate additional low-frequency harmonics in the system which will interact with injected xy voltages, thereby distorting the voltage regulation and might even lead to system misbehavior. Therefore, the linear modulation range is used as the effective restraint in this analysis.

IV. Experimental Validation of Modulation Restraint

Firstly in this section, an open-loop experiment tests the modulation restraints of three SVPWM techniques through voltage injection, in which $\boldsymbol{V}_{xy}^{*}$ can be within and out of the linear modulation range of xy subspace under a given m. Then, a closed-loop current compensation using the PIR(PI+Resonant) controllers under the condition of a series 3.3Ω resistor in Phase R is conducted to show the deterioration of current control with SVPWM-D3 and the enhanced SVPWM-SV out of their modulation restraints. The purpose of the series 3.3Ω resistor is to create a large voltage requirement in xy subspace.

The low-speed direct-drive wind power test rig to conduct the experiments of the voltage injection and current control is

shown in Fig. 20. The test dual 3-ph PMSM with parameters shown in Table IV can be driven by a 3-ph PMSM load machine to rotate at a fixed speed.

TABLE IV
PARAMETERS OF TEST DUAL 3-PH PMSM

Parameters	Value
Rated power	3.7kW
Rated speed	170r/min
Rated torque	209Nm
Stator self-inductance	17.21mH
Stator resistance	3.3Ω
PM Flux	1.03Wb
Number of pole pairs	16

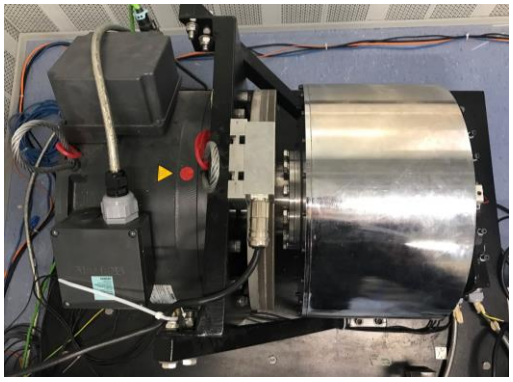

Fig. 20 Test rig setup containing load machine (left) and test dual 3-ph PMSM (right).

A. *Open-loop Voltage Injection*

The control diagram of the open-loop voltage injection is presented in Fig. 21. The dc-link voltage V_{dc} is set to 70V and a fixed mechanical speed of 10 r/min is provided by the load machine. The voltage references u_d^*, u_q^*, u_x^*, u_y^* ($\boldsymbol{V}_{\boldsymbol{\alpha\beta}}^*$, $\boldsymbol{V}_{\boldsymbol{xy}}^*$) are injected as an open-loop control to check whether SVPWM-4L, SVPWM-D3, and the enhanced SVPWM-SV can provide a required modulation of harmonic voltage injection in xy subspace under a given m.

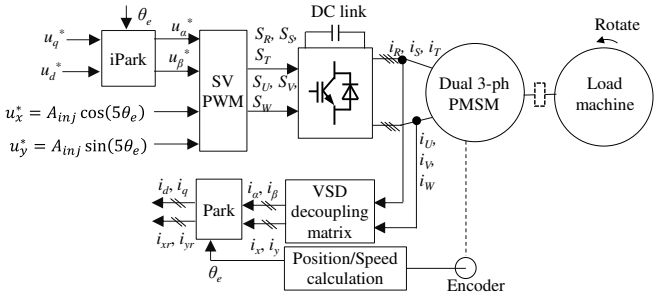

Fig. 21 Control diagram of open-loop voltage injection.

Of note, u_d^* and u_q^* denote voltage references in αβ subspace after Park transform, which are set to $u_d^* = 0$, $u_q^* = 28\text{V}$, achieving $\boldsymbol{V}_{\boldsymbol{\alpha\beta}}^*$ rotating with a magnitude of 28V and resulting in $m = 0.8$ and $L_{LMR} = 12.41$ V according to (9), (10) and (32) for both SVPWM-D3 and the enhanced SVPWM-SV. For u_x^* and u_y^*, the 5th harmonic with an amplitude of A_{inj} is used to test the linear modulation range shown in Fig. 19(a). Of note, other order harmonics can be injected as well since the amplitude matters.

For SVPWM-4L, the voltage trajectories with $A_{inj} = 0$ and 5V are shown in Fig. 22 and Fig. 23, respectively. Since SVPWM-4L has no linear modulation range, the voltage trajectories in both αβ and xy subspaces cannot follow the voltage references with $A_{inj} = 5\,\text{V}$, shown in Fig. 23, confirmed the previous analysis. Meanwhile, the overmodulation based on (12) is activated. Any negative value among T_{SA}, T_{SB}, T_{SC} and T_{SD} would be set to zero. If $T_z < 0$, T_{SA}, T_{SB}, T_{SC} and T_{SD} will reduce proportionally until $T_z = 0$.

Then, for SVPWM-D3 and the enhanced SVPWM-SV, the voltage trajectories with $A_{inj} = 12.41\text{V}$ and 20V are shown in Fig. 24, Fig. 25 and Fig. 26, Fig. 27, respectively. For $A_{inj} = 12.41\text{V}$, both SVPWM-D3 and the enhanced SVPWM-SV can provide a good tracking performance of voltage references but fail at $A_{inj} = 20\text{V}$, which is out of the linear modulation range and leads to the overmodulation. For SVPWM-D3, the overmodulation for 3-ph SVPWM is activated in two sets, respectively. The modulation of any voltage references ($\boldsymbol{V}_{\boldsymbol{\alpha 1\beta 1}}^*$ and $\boldsymbol{V}_{\boldsymbol{\alpha 2\beta 2}}^*$) exceeding the dotted hexagon (described in Fig. 4) will be shortened to the edge of the dotted hexagon with the same direction. The resulting voltage vector will not be the same as its reference in aspects of length and direction in each subspace. For the enhanced SVPWM-SV, the overmodulation is based on (28). If $T_0 = T_{63} < 0$, T_{SV1}, T_{SV2}, T_{SV3} and T_{SV4} will reduce proportionally until $T_z = 0$. Due to the synthetic vectors, the resulting voltage vector after the overmodulation is shorter than its reference in each subspace, but they are in the same direction. As can be seen in Fig. 25 and Fig. 27, for one sampling point, $\boldsymbol{V}_{\boldsymbol{\alpha\beta}}^* = [26.8 \quad -8.14]^{\text{T}}$ ($\frac{u_\beta^*}{u_\alpha^*} = -0.304$), $\boldsymbol{V}_{\boldsymbol{xy}}^* = [-19.9 \quad -1.93]^{\text{T}}$ ($\frac{u_y^*}{u_x^*} = 0.0971$), the resulting voltages after the overmodulation procedure are $\boldsymbol{V}_{\boldsymbol{\alpha\beta}} = [23.6 \quad -7.40]^{\text{T}}$ ($\frac{u_\beta}{u_\alpha} = -0.314$), $\boldsymbol{V}_{\boldsymbol{xy}} = [-16.8 \quad -1.32]^{\text{T}}$ ($\frac{u_y}{u_x} = 0.0782$) and $\boldsymbol{V}_{\boldsymbol{\alpha\beta}} = [23.0 \quad -6.97]^{\text{T}}$ ($\frac{u_\beta}{u_\alpha} = -0.304$), $\boldsymbol{V}_{\boldsymbol{xy}} = [-17.1 \quad -1.66]^{\text{T}}$ ($\frac{u_y}{u_x} = 0.0971$) for SVPWM-D3 and the enhanced SVPWM-SV, respectively. It can be seen that the resulting voltage vector is shorter than its reference in each subspace for the two SVPWM techniques. However, the directions for the resulting voltage vector and its reference are different for SVPWM-D3.

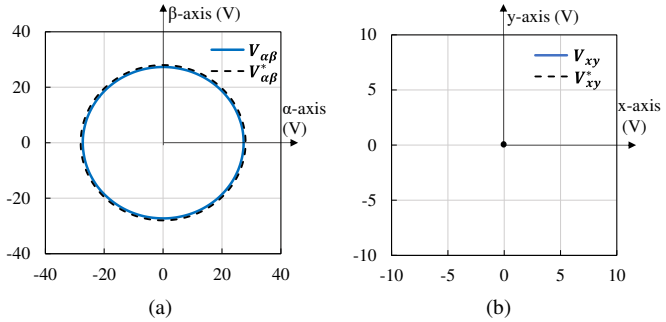

Fig. 22 Voltage trajectories with $A_{inj} = 0$ for SVPWM-4L. (a) αβ subspace. (b) xy subspace.

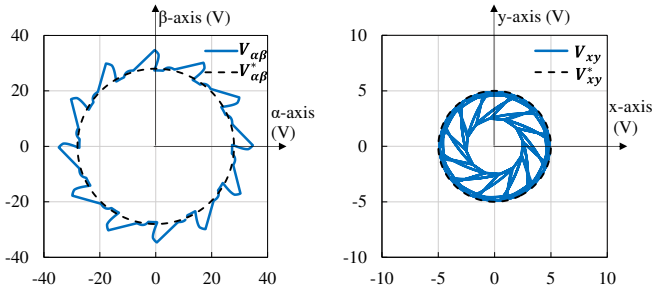

Fig. 23 Voltage trajectories with $A_{inj} = 5$V for SVPWM-4L. (a) αβ subspace. (b) xy subspace.

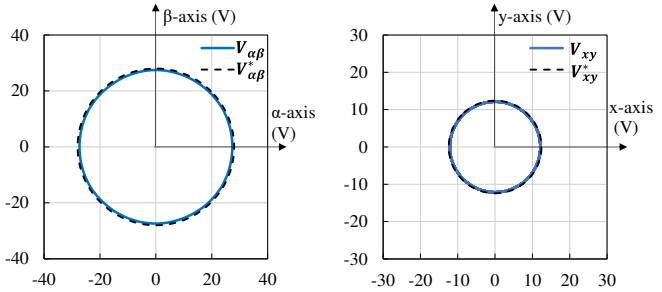

Fig. 24 Voltage trajectories with $A_{inj} = 12.41$V for SVPWM-D3. (a) αβ subspace. (b) xy subspace.

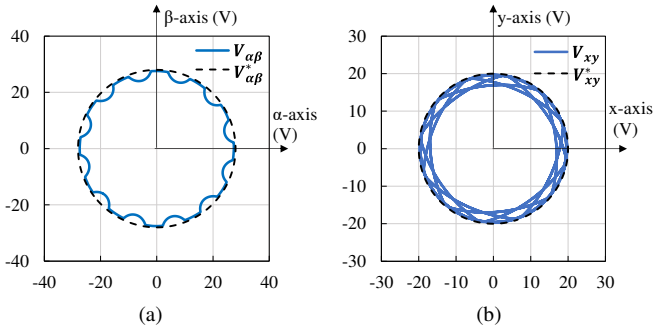

Fig. 25 Voltage trajectories with $A_{inj} = 20$V for SVPWM-D3. (a) αβ subspace. (b) xy subspace.

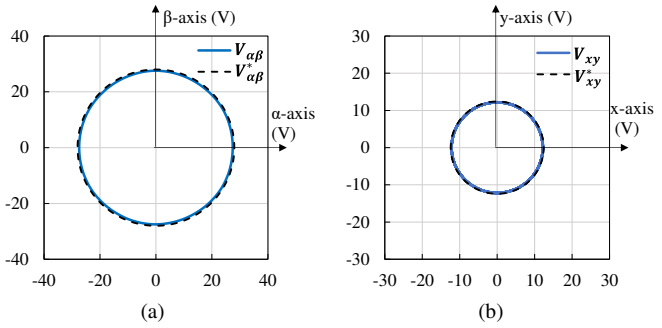

Fig. 26 Voltage trajectories with $A_{inj} = 12.41$ V for enhanced SVPWM-SV. (a) αβ subspace. (b) xy subspace.

B. Closed-loop Current Compensation

The closed-loop current compensation shown in Fig. 28 could be more common and practical in xy subspace regulation, in which $G_R(s)$ denoting the transfer function of the resonant controller is illustrated later. As mentioned in the introduction section, currents in xy subspace should be suppressed to zero to improve the system performances. To create a high demand for voltage in xy subspace to test the linear modulation range, a series 3.3 Ω resistor causing unbalanced phase currents is connected to Phase R. Through adjusting the dc-link voltage, the magnitude of voltage reference in xy subspace required for balancing phase currents can be out of the linear modulation range. Then, the deterioration of current compensation restricted by the linear modulation range can be tested. With the additional resistor, (1) is changed as

$$\begin{bmatrix} u_\alpha \\ u_\beta \\ u_x \\ u_y \end{bmatrix} = \begin{bmatrix} \frac{4}{3}R_s & 0 & \frac{1}{3}R_s & 0 \\ 0 & R_s & 0 & 0 \\ \frac{1}{3}R_s & 0 & \frac{4}{3}R_s & 0 \\ 0 & 0 & 0 & R_s \end{bmatrix} \begin{bmatrix} i_\alpha \\ i_\beta \\ i_x \\ i_y \end{bmatrix} + \begin{bmatrix} \dot{\psi}_\alpha \\ \dot{\psi}_\beta \\ \dot{\psi}_x \\ \dot{\psi}_y \end{bmatrix}. \tag{33}$$

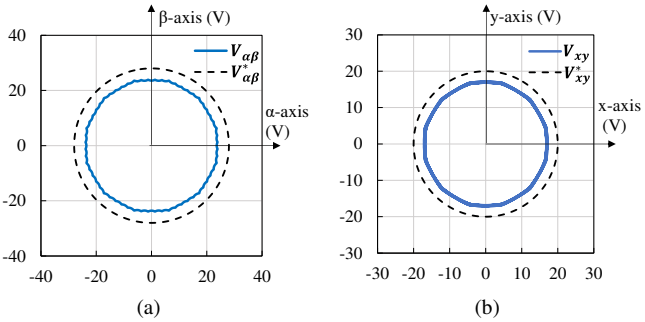

Fig. 27 Voltage trajectories with $A_{inj} = 20$V for enhanced SVPWM-SV. (a) αβ subspace. (b) xy subspace.

From (33), the additional resistor leads to the cross-coupling between α-axis and x-axis, which means a fundamental component in i_x can be caused by i_α if no compensation, i.e. $u_x = u_y = 0$. Therefore, a large voltage demand is created to regulate currents in a good performance, expressed as

$$\begin{bmatrix} i_\alpha \\ i_\beta \\ i_x \\ i_y \end{bmatrix} = \begin{bmatrix} i_d\cos(\theta_e) - i_q\sin(\theta_e) \\ i_d\sin(\theta_e) + i_q\cos(\theta_e) \\ 0 \\ 0 \end{bmatrix}, \tag{34}$$

in which, i_d and i_q denote the d-axis and q-axis currents, respectively, after Park transform in αβ subspace. Setting i_d to zero, the voltage demand for the compensation of the fundamental current in xy subspace is $\frac{1}{3}R_s \cdot i_q\sin(\theta_e)$ calculated from (33) and (34). Of note, the 5th and 7th current harmonics decoupled in xy subspace require a compensation voltage as well so that the voltage reference in xy subspace should cover the mitigation of these current harmonics.

Then, how the voltage reference in xy subspace is generated to compensate the fundamental, 5th and 7th harmonic components is illustrated. The closed-loop current control diagram with the purpose of controlling i_x and i_y to zero is presented in Fig. 28, in which i_{xr}, i_{yr} and u_{xr}, u_{yr} denote currents and voltages after Park transform in xy subspace. After Park transform, 5th and 7th harmonics are converted into 6th

[11] and the fundamental component appears as DC component and 2nd harmonics. Then, the PIR controllers [11], [21]-[22] are implemented to generate the voltage references suppressing current harmonics, since the resonant controller can offer a large gain at the frequencies of $2\omega_s$ and $6\omega_s$ (ω_s denotes fundamental frequency). The transfer function of the applied resonant controller can be expressed as

$$G_R(s) = \frac{K_r s}{s^2 + \omega_c s + (h\omega_s)^2}, \tag{35}$$

where K_r denotes the resonant gain; h denotes the order; ω_c denotes cut-off frequency, which determines the bandwidth regarding the resonant frequency [22]. Details of parameter tuning can be seen in [21]-[22], since PIR controllers are not within the research scope of this paper. In the experiments, the parameters are listed in Table V and the output limit of PIR controllers is set to $\frac{V_{dc}}{\sqrt{3}}$.

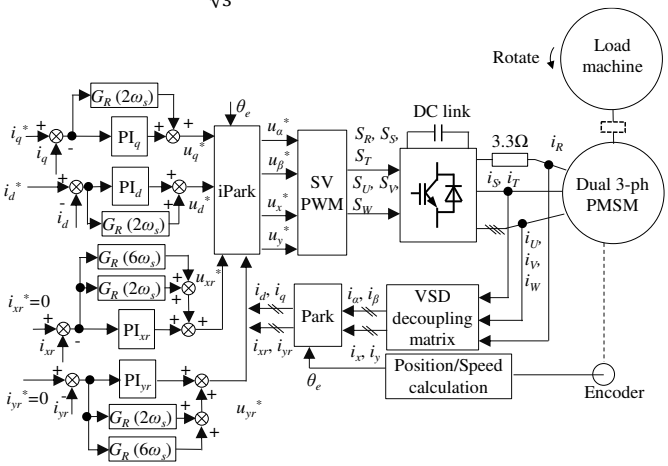

Fig. 28 Control diagram of closed-loop current compensation.

TABLE V
PARAMETERS OF PIR CONTROLLERS

i_d/i_q PIR controllers		i_{xr}/i_{yr} PIR controllers	
Parameter	Value	Parameter	Value
K_p	45	K_p	12
K_i	2750	K_i	2750
K_r	2750	K_r	2750
ω_c	$\omega_s/50$	ω_c	$\omega_s/50$

The speed of the test machine is driven to 10 r/min by the load machine. Substituting (33), (34) into (9) and neglecting harmonics with much smaller amplitudes, the linear modulation ranges for SVPWM-D3 and the enhanced SVPWM-SV against i_q under V_{dc}=50V and 70V are plotted in Fig. 29. It can be seen that under the condition of i_q =2.5A and V_{dc}=50V (70V), L_{LMR} is 0.59V (12.14V). However, substituting (34) into (33), the maximum magnitude of $\boldsymbol{V}_{\boldsymbol{xy}}^*$ required to suppress this fundamental component without considering the low-amplitude 5th and 7th harmonics in xy subspace can be estimated around 2.75V which is larger than L_{LMR} for V_{dc}=50V, but smaller than L_{LMR} for V_{dc} =70V. There is still a large margin for the compensation of 5th and 7th harmonics under V_{dc}=70V. Thus, the suppression in xy subspace can be achieved by SVPWM-D3 and the enhanced SVPWM-SV under V_{dc}=70V, but fails under V_{dc}=50V, thereby demonstrating the deterioration of current compensation out of the SPVWM modulation restraints.

The experimental results using only PI controllers in αβ subspace (no compensation in xy subspace, i.e. $u_x^* = 0, u_y^* = 0$) under i_d^* =0, i_q^* =2.5A and V_{dc}=70V are presented in Fig. 30 to show the unbalanced phase currents and the current in xy subspace caused by the series 3.3Ω resistor in Phase R. The voltage trajectories in αβ and xy subspaces are shown in Fig. 30(a) and (b), respectively, calculated from the duty cycles shown in Fig. 30(c). From Fig. 30(d), the phase currents are unbalanced, leading to a large fundamental component in the x-axis current, shown in Fig. 30(g). The spectrum analysis of Phase R and U currents are presented in Fig. 30(e) and the fundamental amplitudes of unbalanced Phase R and U currents reach 1.98A and 2.95A, respectively. Meanwhile, the 5th and 7th harmonics caused by inverter nonlinearities are presented as well due to no compensation in xy subspace. The spectrum analysis of i_x and i_y shown in Fig. 30(h) validates (33) and a requirement of compensation for the 5th and 7th harmonics in xy subspace.

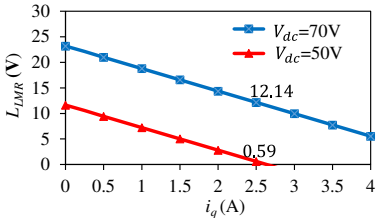

Fig. 29 L_{LMR} against i_q for SVPWM-D3 and enhanced SVPWM-SV.

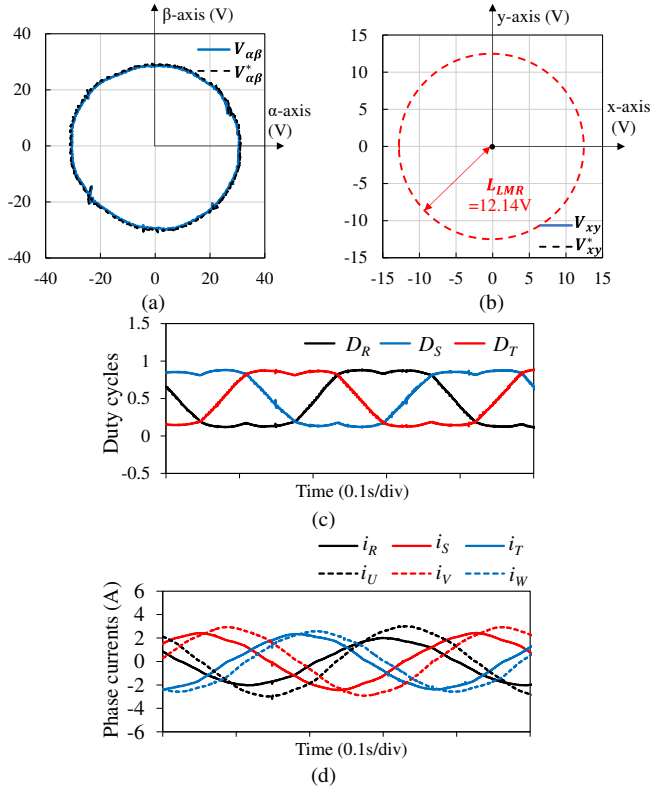

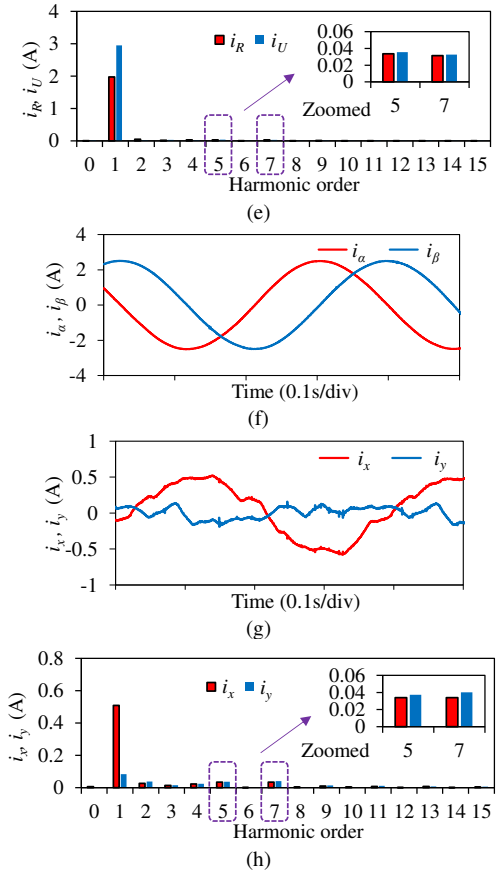

Fig. 30 Experimental results without current compensation in xy subspace using SVPWM-D3 under V_{dc}=70V. (a) Voltage trajectory in αβ subspace. (b) Voltage trajectory in xy subspace. (c) Duty cycles. (d) Phase currents. (e) Spectrum analysis of Phase R and U currents. (f) Currents in αβ subspace. (g) Currents in xy subspace. (h) Spectrum analysis of currents in xy subspace.

Then, the experimental results with current compensation in xy subspace using SVPWM-D3 under V_{dc}=70V are presented in Fig. 31. The voltage trajectory in xy subspace, shown in Fig. 31(b) indicates the voltage reference is within the linear modulation range, therefore, SVPWM-D3 can modulate voltage references in both subspaces illustrated in Fig. 31(a) and (b). Due to the control of xy subspace, currents are well regulated as shown in Fig. 31(d), (f) and (g). The spectrum analysis of Phase R and U presented in Fig. 31(e) shows that the fundamental components are balanced and the 5th/7th harmonics are suppressed effectively. From Fig. 31(g), i_x and i_y are controlled to zero.

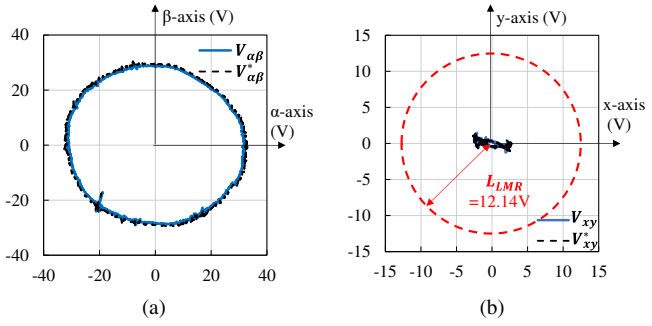

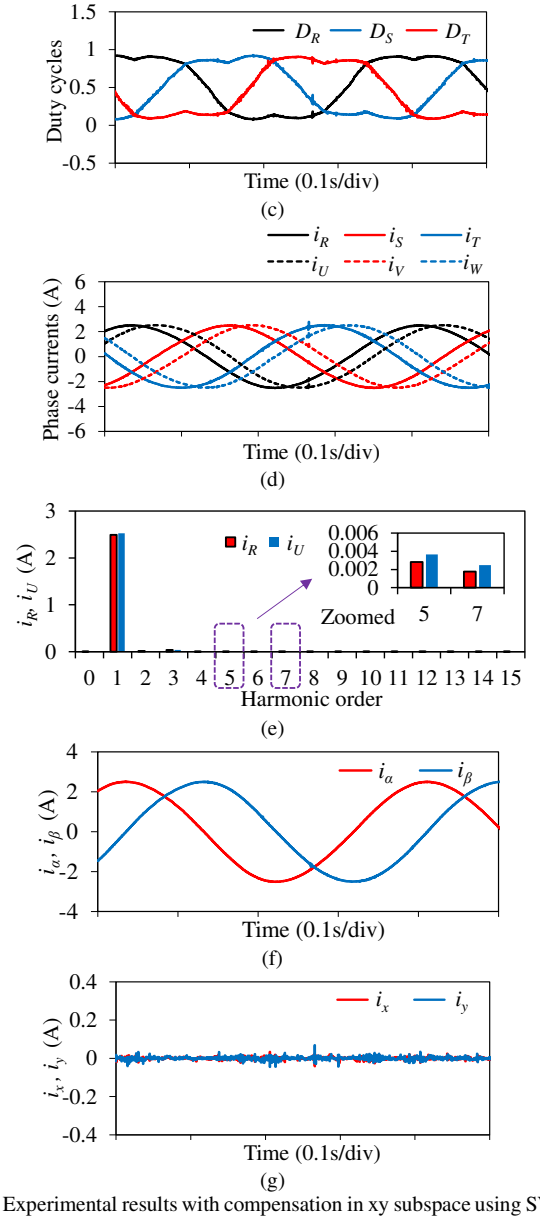

Fig. 31 Experimental results with compensation in xy subspace using SVPWM-D3 under V_{dc}=70V. (a) Voltage trajectory in αβ subspace. (b) Voltage trajectory in xy subspace. (c) Duty cycles. (d) Phase currents. (e) Spectrum analysis of Phase R and U currents. (f) Currents in αβ subspace. (g) Currents in xy subspace.

On the contrary, V_{dc} =50V cannot satisfy the voltage requirement of compensation in xy subspace, as in Fig. 32. From Fig. 32(b), the reference in xy subspace is out of the linear modulation range and leads to the voltage tracking failures in both subspaces (Fig. 32(a) and (b)). The saturation of duty cycles is shown in Fig. 32(c). Meanwhile, the voltage references could conduct misbehavior and reach the output limit of current controllers as indicated in Fig. 32(a) and (b). Thus, the currents are distorted as shown in Fig. 32(d), (f) and (g). From the spectrum analysis of Phase R and U shown in Fig. 32(e), the modulation failure (or the overmodulation) reduces the amplitudes of fundamental components in Phase R and Phase U currents from 2.49A and 2.52A (shown in Fig. 31(e)) to 1.85A and 1.88A, respectively, which means the current references

i_d^* =0, i_q^* =2.5A are not satisfied and followed. Meanwhile, the compensation of the 5th and 7th harmonics is deteriorated.

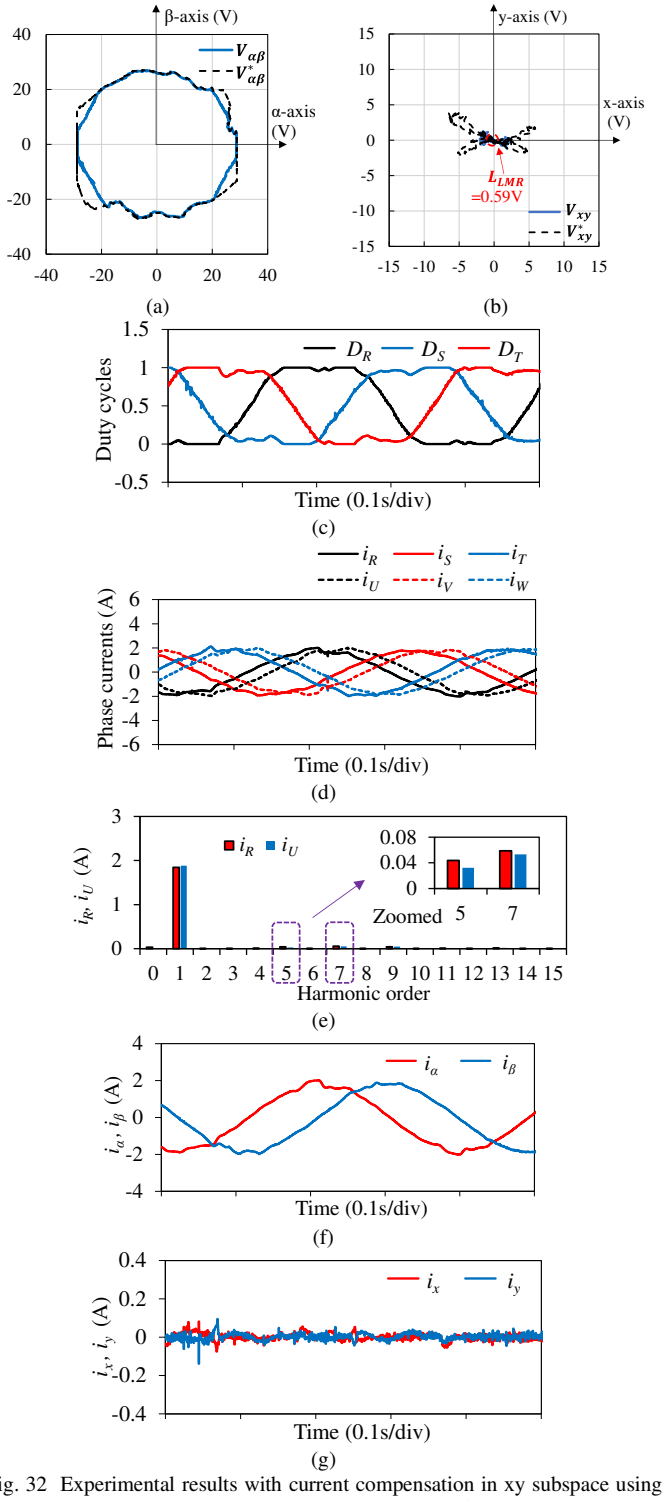

Fig. 32 Experimental results with current compensation in xy subspace using SVPWM-D3 under V_{dc}=50V. (a) Voltage trajectory in αβ subspace. (b) Voltage trajectory in xy subspace. (c) Duty cycles. (d) Phase currents. (e) Spectrum analysis of Phase R and U currents. (f) Currents in αβ subspace. (g) Currents in xy subspace.

The experimental results with current compensation in xy subspace using the enhanced SVPWM-SV under V_{dc}=70V and 50V are presented in Fig. 33 and Fig. 34, respectively. Under V_{dc} =70V, the voltage required for the compensation in xy subspace is within the linear modulation range, illustrated in Fig. 33(b). Therefore, the currents can be well regulated, as shown in Fig. 33(d), (f), and (g). However, the enhanced SVPWM-SV fails to provide the modulation of voltage references in xy subspace, which is out of the linear modulation range under V_{dc}=50V, thereby distorting the current balancing, presented in Fig. 34. Comparing the spectrum analysis of Phase R and Phase under V_{dc}=70V and V_{dc}=50V shown in Fig. 33(e) and Fig. 34(e), the amplitudes of fundamental components of Phase R and U are reduced to 1.77A and 1.80A under V_{dc}=50V from 2.49A and 2.52A under V_{dc}=70V, respectively. It means that the current references i_d^* =0, i_q^* =2.5A are not fulfilled under V_{dc}=50V. Also, the 5th/7th harmonic compensation is affected by the modulation failure.

Comparing Fig. 32 and Fig. 34, the enhanced SVPWM-SV performs slightly better than SVPWM-D3 with limited dc-link voltage. Regarding SVPWM techniques, the overmodulation procedure and the nonlinear modulation range are the two main factors determining the performance with the voltage reference out of the linear modulation range. As shown in the last paragraph of Section IV-A, the overmodulation procedures of both SVPWM-D3 and the enhanced SVPWM-SV could lead to different resulting voltage vectors. The direction of the resulting voltage vector could be different from that of its reference for SVPWM-D3. On the other hand, the different nonlinear modulation ranges of these two SVPWM techniques could generate different low-frequency harmonics, thereby affecting the performance. Of note, under other voltage references involving harmonics with different orders, amplitudes or phases in xy subspace, the performance for SVPWM-D3 and the enhanced SVPWM-SV could vary. Therefore, it cannot be guaranteed that one technique has a better performance than the other for any voltage reference with limited dc-link voltage. This is our future research direction.

For both SVPWM techniques, the modulation of the fundamental voltage in αβ subspace deteriorates due to the limited dc-link voltage. However, it might need to be secured in most applications because of the electromagnetic torque control. Under the condition of limited dc-link voltage, the partial control strategy can be applied to secure the modulation in αβ subspace for both SVPWM-D3 and the enhanced SVPWM-SV. In this approach, the length of $\boldsymbol{V}^*_{\boldsymbol{xy}}$ is reduced to L_{LMR} but the direction of $\boldsymbol{V}^*_{\boldsymbol{xy}}$ does not change. Therefore, the control in xy subspace can be achieved partially.

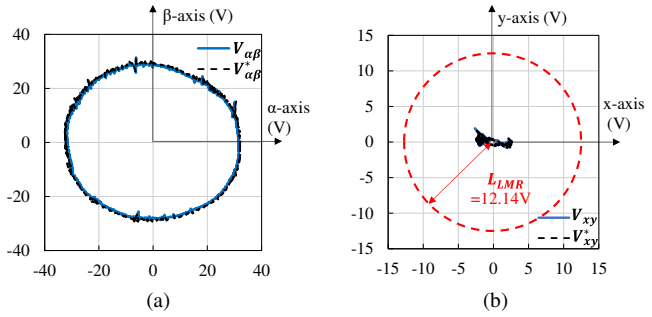

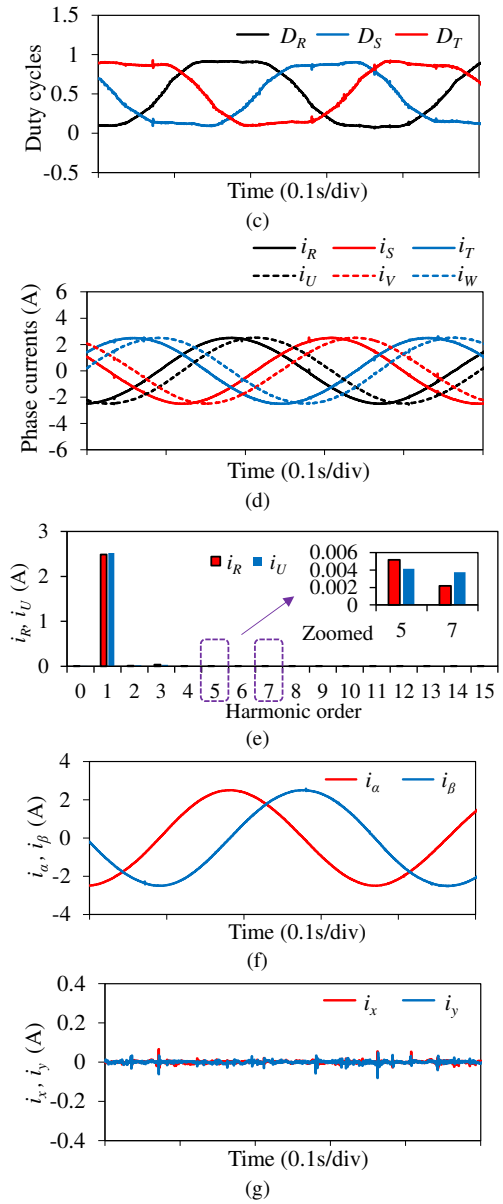

Fig. 33 Experimental results with current compensation in xy subspace using enhanced SVPWM-SV under V_{dc}=70V. (a) Voltage trajectory in αβ subspace. (b) Voltage trajectory in xy subspace. (c) Duty cycles. (d) Phase currents. (e) Spectrum analysis of Phase R and U currents. (f) Currents in αβ subspace. (g) Currents in xy subspace.

V. Conclusion

This paper focuses on the modulation restraint analysis of three practical SVPWM techniques for dual 3-ph machines under vector space decomposition, through defining the linear modulation range of xy subspace under an assured modulation index of fundamental voltage. It is found that there is no linear modulation range in xy subspace for the SVPWM with four large voltage vectors, while there is a trade-off between the linear modulation range of xy subspace and the modulation index of fundamental voltage in αβ subspace for the SVPWM with two separate 3-ph modulation frames and the SVPWM with synthetic vectors which is further enhanced in this work by reducing the device switching frequency. This is particularly useful to limit the output limit of current controllers in xy subspace (harmonic control capability) under a required electromagnetic toque or current, thereby avoiding the modulation failure.

The experimental results in the open-loop voltage injection and the closed-loop current compensation demonstrate the voltage distortion, failure of current regulation, and harmonics caused by the modulation failure when the voltage reference in xy subspace exceeds the linear modulation range.

Besides, the three SVPWM techniques are generally representative regarding the voltage vector selection principle, so that other SVPWM techniques using similar voltage vector selection principles can be analyzed following the procedures presented in this paper. Additionally, the SVPWM using synthetic vectors is improved to be simpler and more practical and accessible for microcontrollers because of no complicated switch sequence arrangement and no multiple switching.

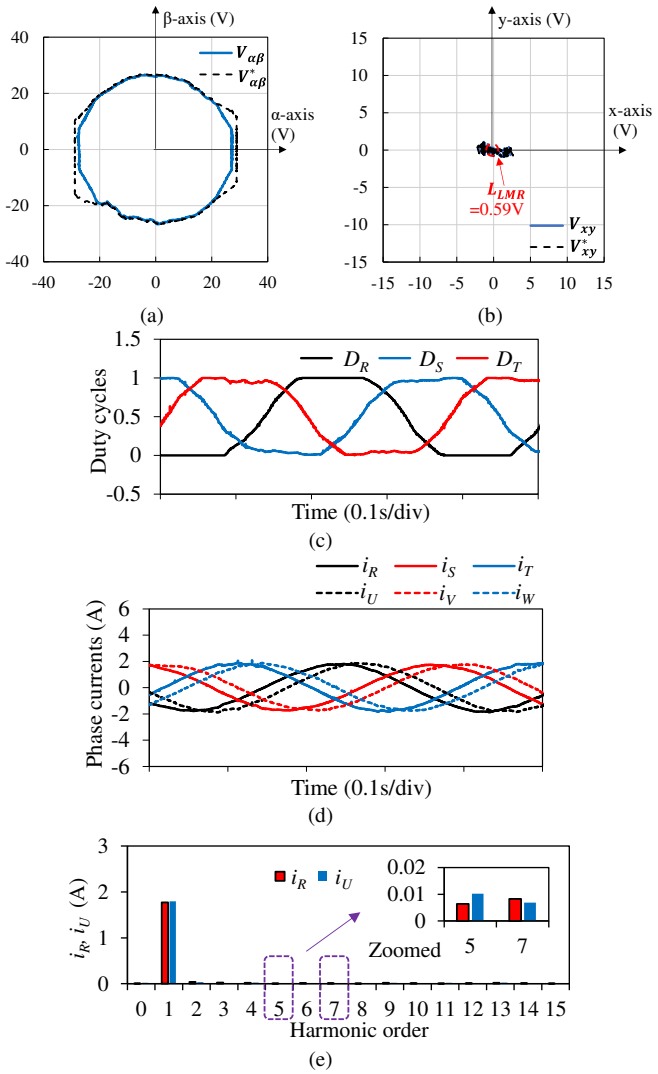

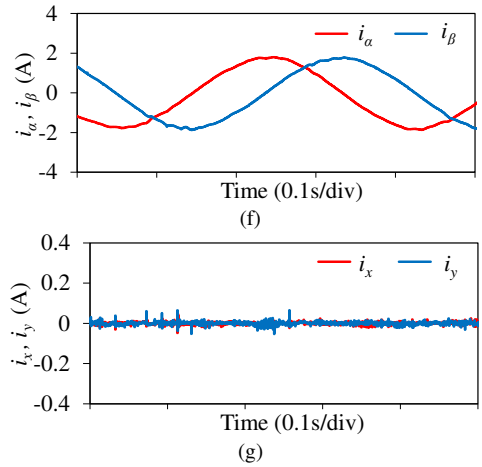

Fig. 34 Experimental results with current compensation in xy subspace using enhanced SVPWM-SV under V_{dc}=50V. (a) Voltage trajectory in αβ subspace. (b) Voltage trajectory in xy subspace. (c) Duty cycles. (d) Phase currents. (e) Spectrum analysis of Phase R and U currents (f) Currents in αβ subspace. (g) Currents in xy subspace.

REFERENCES

[1] E. Levi, "Advances in converter control and innovative exploitation of additional degrees of freedom for multiphase machines," *IEEE Trans. Ind. Electron.*, vol. 63, no. 1, pp. 433–448, Jan. 2016.

[2] R. Bojoi, S. Rubino, A. Tenconi, and S. Vaschetto, "Multiphase electrical machines and drives: A viable solution for energy generation and transportation electrification," in *Proc. Int. Conf. Expo. Elect. Power Eng.*, 2016, pp. 632–639.

[3] C. A. Reusser, S. Kouro, and R. Cardenas, "Dual three-phase PMSG based wind energy conversion system using 9-switch dual converter," in *Proc. IEEE Energy Convers. Congr. Expo.*, 2015, pp. 1021-1022.

[4] K. Y. Hwang, B. K. Song, and B. I. Kwon, "Asymmetric dual winding three-phase PMSM for fault tolerance of overheat in electric braking system of autonomous vehicle," *IET Elect. Power Appl.*, vol. 13, no. 12, pp. 1891-1898, Dec. 2019.

[5] S. Hu, Z. Liang, W. Zhang, and X. He, "Research on the integration of hybrid energy storage system and dual three-phase PMSM drive in EV," *IEEE Trans. Ind. Electron.*, vol. 65, no. 8, pp. 6602–6611, Aug. 2018.

[6] J. Nerg, M. Rilla, V. Ruuskanen, J. Pyrhonen, and S. Ruotsalainen, "Direct-driven interior magnet permanent-magnet synchronous motors for a full electric sports car," *IEEE Trans. Ind. Electron.*, vol. 61, no. 8, pp. 4286–4294, Aug. 2014.

[7] Y. He, Y. Wang, J. Wu, Y. Feng, and J. Liu, "A simple current sharing scheme for dual three-phase permanent-magnet synchronous motor drives," in *Proc. Annu. IEEE Appl. Power Electron. Conf. Expo.*, 2010, pp. 1093–1096.

[8] R. O. C. Lyra and T. A. Lipo, "Torque density improvement in a six-phase induction motor with third harmonic current injection," *IEEE Trans. Ind. Appl.*, vol. 38, no. 5, pp. 1351-1360, Sep.-Oct. 2002.

[9] Y. Zhao and T. Lipo, "Space vector PWM control of dual three-phase induction machine using vector space decomposition," *IEEE Trans. Ind. Appl.*, vol. 31, no. 5, pp. 1100–1109, Sep. 1995.

[10] A. H. Abosh, Z. Q. Zhu, and Y. Ren, "Reduction of torque and flux ripples in space vector modulation-based direct torque control of asymmetric permanent magnet synchronous machine," *IEEE Trans. Power Electron.*, vol. 32, no. 4, pp. 2976-2986, Apr. 2017.

[11] H. S. Che, E. Levi, M. Jones, W. P. Hew, and N. Abd Rahim, "Current control methods for an asymmetrical six-phase induction motor drive," *IEEE Trans. Power Electron.*, vol. 29, no. 1, pp. 407–417, Jan. 2014.

[12] D. Hadiouche, L. Baghli, and A. Rezzoug, "Space-vector PWM techniques for dual three-phase AC machine: analysis, performance evaluation, and DSP implementation," *IEEE Trans. Ind. Appl.*, vol. 42, no. 4, pp. 1112-1122, Jul.-Aug. 2006.

[13] K. Marouani, L. Baghli, D. Hadiouche, A. Kheloui, and A. Rezzoug, "Discontinuous SVPWM techniques for double star induction motor drive control," in *Proc. Annu. Conf. IEEE Ind. Electron.*, 2006, pp. 902-907.

[14] D. Hadiouche, H. Razik, and A. Rezzoug, "Study and simulation of space vector PWM control of double-star induction motors," in *Proc. IEEE Int. Power Electron. Cong.*, 2000, pp. 42-47.

[15] K. Marouani, L. Baghli, D. Hadiouche, A. Kheloui, and A. Rezzoug, "A new PWM strategy based on a 24-sector vector space decomposition for a six-phase VSI-Fed dual stator induction motor," *IEEE Trans. Ind. Electron.*, vol. 55, no. 5, pp. 1910–1920, May 2008.

[16] A. R. Bakhshai, G. Joos, and H. Jin, "Space vector PWM control of a split-phase induction machine using the vector classification technique," in *Proc. IEEE Appl. Power Electron. Conf. Expo.*, 1998, vol. 2, pp. 802-808.

[17] J. Xu, M. Odavic, and Z. Zhu, "An advanced harmonic compensation strategy for dual three-phase permanent magnet synchronous machines considering different angle displacements," in *Proc. IEEE Energy Convers. Congr. Expo.*, 2019, pp. 1797-1803.

[18] Y. Hu, Z. Q. Zhu, and M. Odavic, "Comparison of two-individual current control and vector space decomposition control for dual three-phase PMSM," *IEEE Trans. Ind. Appl.*, vol. 53, no. 5, pp. 4483–4492, Sep. 2017.

[19] Y. Hu, Z. Q. Zhu, and M. Odavic, "Torque capability enhancement of dual three-phase pmsm drive with fifth and seventh current harmonics injection," *IEEE Trans. Ind. Appl.*, vol. 53, no. 5, pp. 4526-4535, Sep.-Oct. 2017.

[20] J. Prieto, J. A. Riveros, and B. Bogado, "Multifrequency output voltage generation for asymmetrical dual three-phase drives," in *Proc. IEEE Int. Elect. Mach. Drives Conf.*, 2017, pp. 1–6.

[21] Y. Hu, Z. Zhu, and K. Liu, "Current control for dual three-phase permanent magnet synchronous motors accounting for current unbalance and harmonics," *IEEE J. Emerg. Sel. Topics Power Electron.*, vol. 2, no. 2, pp. 272-284, Jun. 2014.

[22] J. Hu, H. Nian, H. Xu, and Y. He, "Dynamic modeling and improved control of DFIG under distorted grid voltage conditions," *IEEE Trans. Energy Convers.*, vol. 26, no. 1, pp. 163–175, Mar. 2011.